Effects of Square Spiral Pitch and Tie Overlap on the Behavior of GFRP-Reinforced Concrete Columns under Concentric and Eccentric Loads

Alireza Sadat Hosseini[1*] and Pedram Sadeghian[2]

[1] Research Assistant, Department of Civil and Resource Engineering, Dalhousie University, Canada

[2] Associate Professor and Canada Research Chair in Sustainable Infrastructure, Department of Civil and Resource Engineering, Dalhousie University, Canada

* Corresponding Author, email: asadat@dal.ca

ABSTRACT

The structural behavior of glass fiber-reinforced polymer (GFRP)-reinforced concrete (RC) columns is studied to evaluate the effects of square spirals and ties under concentric and eccentric loading. An experimental program was conducted on fifteen specimens with varied configurations, including spiral pitches, tie spacing and overlap lengths, and reinforcement ratio, to evaluate their impact on confinement, load-bearing capacity, and deformability. Results indicated that GFRP bars contributed between 7% and 15% of load-bearing capacity, while steel reinforcement contributed approximately 30%. Under concentric loading, a denser spiral pitch increased the peak load by about 6%, though spiral pitch had minimal effect on peak loads under eccentric loading. In both loading types, columns with denser spirals exhibited a more gradual post-peak load decline. Whereas under eccentric loading, larger spiral pitches led to a more brittle failure pattern, often resulting in the crushing of compressive bars. In specimens with ties, increasing the tie overlap length by 40% above the code minimum shifted the failure mode from sudden, crack-free failure to gradual post-peak failure. An analytical model was developed and validated using data from the experiment in this study and from the literature. The model accurately predicted load-displacement and strain behavior across various eccentricities.

DOI: https://doi.org/10.1016/j.istruc.2025.108947

Keywords: GFRP; Square Spiral; Reinforced Concrete Column; Load Eccentricity; confinement

1. INTRODUCTION

Square spirals are continuous transverse reinforcement for columns with a square cross-section. The significance of Glass Fiber Reinforced Polymer (GFRP) square spirals in reinforced concrete (RC) columns lies in their potential to enhance durability, ease of construction, and overall structural performance. Unlike conventional steel reinforcement, GFRP does not corrode, making it especially attractive for applications in aggressive environments—such as coastal regions, marine structures, bridge piers, and infrastructure exposed to de-icing salts or chemicals. In addition, GFRP spirals contribute to sustainability by reducing maintenance requirements and extending the service life of concrete structures, while their lightweight nature simplifies transportation and handling during construction. From a structural perspective, GFRP square spirals provide passive confinement to the concrete core by restraining lateral expansion under axial loads. This confinement improves ductility, energy absorption, and the overall resilience of the column. However, to fully harness these benefits, it is essential to investigate their behavior under various configurations and loading conditions.

The behavior of concentrically loaded GFRP-reinforced concrete (GFRP-RC) columns has been extensively studied to understand the contribution of GFRP bars to column capacity. Findings suggest that GFRP bars offer varying contributions, with studies by Afifi et al. [1] and De Luca et al. [2] indicating an average load contribution of 5–10% and less than 5%, respectively, compared to steel's 12%. Afifi et al. demonstrated that ignoring GFRP's contribution can lead to a 35% underestimation of load capacity, while Hadhood et al. [3], [4] emphasized the brittle concrete crushing as the primary failure mode in GFRP-reinforced circular columns. The stiffness of cracked concrete sections was effectively enhanced with GFRP reinforcement, although increasing the longitudinal reinforcement ratio did not significantly affect behavior under concentric loads.

Studies on high-strength concrete columns by Hadi et al. [5] highlighted a 30% reduction in ductility compared to steel-reinforced columns. Khorramian and Sadeghian [6] tested GFRP-RC columns and no GFRP bar crushing was observed before the peak load, with GFRP strains staying below half of their ultimate strain. Although GFRP contributes less to the column's capacity compared to steel bars, it supports the axial load without failing until the peak load is reached [7], [8], [9].

The effect of eccentricity on GFRP-RC columns highlights varied conclusions regarding the role of GFRP bars under eccentric axial loads. While some researchers, including Elchalakani and Ma [10] and Sun et al. [11], suggest disregarding GFRP's contribution under eccentric loading, others argue that GFRP bars meaningfully support columns under such conditions. Studies by Khorramian and Sadeghian [6] and Guérin et al. [12] [13] demonstrate that GFRP bars contribute to enhanced ductility and strength under eccentric loading. Hadhood et al. [14] observed that CFRP-RC columns mirrored the behavior of steel-RC columns up to peak loads, with only a minor reduction in load capacity under high eccentricity.

Research on lateral reinforcement has focused on spiral and tie configuration, spacing, and the impact on confinement efficiency. Afifi et al. [1] [15] [16] found that smaller-diameter spirals with closer spacing improved ductility and reduced the likelihood of diagonal shear failure, particularly for CFRP-RC columns. Further, De Luca et al. [2] indicated that failure modes were largely influenced by tie spacing, though peak capacity was unaffected. Guérin et al. [12] [13] found that using GFRP ties effectively prevented buckling of longitudinal reinforcement, especially with spacing reduced to half of ACI 318-14's recommendations. Likewise, Elchalakani and Ma [10] observed that GFRP columns achieved 93.5% of steel columns' axial load capacity but tie spacing limited GFRP's overall effectiveness. The efficacy of GFRP spirals and hoops in confining the concrete core has been supported by Hadhood et al. [14] and Mohamed et al. [9], where tightly spaced GFRP helices provided superior confinement even post-peak. Tobbi et al. [17] [18] found that tie configuration and spacing were critical for achieving strength and ductility gains, noting that closed GFRP ties outperformed C-shaped ones in confinement efficiency. Based on test results on square RC columns with GFRP and CFRP ties, Tobbi [19] observed that FRP ties significantly enhanced concrete strength and ductility. However, closed FRP ties showed superiority over C-shaped ones in terms of confinement effectiveness. Ali and El-Salakawy [20] observed that columns with well-distributed longitudinal reinforcement and closely-spaced ties demonstrated significant energy absorption, with GFRP-RC specimens absorbing approximately half the energy of steel-RC columns. Tests by Maranan et al. [8] showed that reducing tie spacing to 50 mm significantly enhanced ductility indices and confinement efficiency. Additionally, Hadi et al. [5] , [7] and Karim et al. [21] observed substantial improvements in ductility under concentric loads when reducing GFRP spirals pitch.

While previous studies have extensively examined the performance of GFRP-RC columns under both concentric and eccentric loading conditions, most of the research has focused on either circular sections or limited configurations of square sections. The influence of square GFRP spirals, particularly with varying pitches and tie configurations, on the behavior of concrete columns under axial loads has not been thoroughly investigated. The role of GFRP spirals in delaying lateral expansion and sustaining confinement under different loading conditions remains underexplored. This study addresses this gap by examining the performance of GFRP square spirals under both concentric and eccentric loads.

GFRP-RC columns with square spirals and ties were tested in various configurations under concentric and eccentric loading. Following that, an analytical model is developed to predict load-displacement response, strain in bars and column loading path, validated against experimental data from this study and the literature. The goal is to determine whether optimized square GFRP spirals or ties can improve confinement and load-bearing capacity, and if continuous transverse reinforcement with spirals provides greater ductility and delayed failure compared to discrete ties for square columns.

2. EXPERIMENTAL PROGRAM

This section details the experimental setup, including specimen layout, materials, instrumentation, and test procedure.

2.1. Specimens Layout

Fifteen GFRP-RC column specimens were fabricated, each with a square cross-section measuring 203 mm per side (8 in) and a length of 1220 mm (4 ft). A uniform concrete cover of 25.4 mm (1 in) was maintained for all specimens. Nine of the specimens were subjected to concentric axial loading, while the remaining six were tested under eccentric loading with two levels of eccentricity: 15% and 30% of the section depth.

Of the concentrically loaded specimens, four were reinforced with square ties as transverse reinforcement. Three of these specimens used GFRP reinforcement for both longitudinal bars and ties, while one specimen was reinforced with steel bars and ties. The other five specimens employed square GFRP spirals as transverse reinforcement, with three specimens varying the spiral pitch (25, 50, and 75 mm) to investigate its influence on structural behavior. Two additional specimens had longitudinal reinforcement ratios of 2% and 4%, compared to the average 3% used for the rest, to evaluate the effect of varying longitudinal reinforcement ratios.

Key experimental variables included spiral pitch, tie spacing, tie overlap length, longitudinal reinforcement ratio, and the type of reinforcement material. The experimental matrix is presented in Table 1. The specimen ID for the specimens follows the format X-Rm-Yn-ei, where "X" represents the reinforcement material (G for GFRP or S for steel), "Rm" denotes the longitudinal reinforcement ratio (m = 2, 3, or 4%), and "Yn" defines the transverse reinforcement configuration, where "Y" indicates the type of transverse reinforcement (S for spiral or T for tie), and "n" specifies different spiral pitches or tie configurations (spacing and/or overlap). The final component, "ei," refers to the eccentricity ratio of the axial load; "i=0" represents concentric tests, whereas "i=15" and "i=30" indicate 15% and 30% eccentricity, respectively.

Table 1 - Test matrix

Number	Specimen ID	Number of longitudinal rebars	ρ_L (%)	Spiral pitch or tie spacing (mm)	Tie overlap (mm)	e/h^* (%)
1	G-R3-S1-e0	6	3	25	N.A.	0
2	G-R3-S2-e0	6	3	50	N.A.	0
3	G-R3-S3-e0	6	3	75	N.A.	0
4	G-R3-T1-e0	6	3	75	203	0
5	G-R3-T2-e0	6	3	190	203	0
6	G-R3-T3-e0	6	3	190	305	0
7	G-R2-S2-e0	4	2	50	N.A.	0
8	G-R4-S2-e0	8	4	50	N.A.	0
9	S-R3-T2-e0	6	3	190	203	0
10	G-R3-S1-e15	6	3	25	N.A.	15
11	G-R3-S2-e15	6	3	50	N.A.	15
12	G-R3-S3-e15	6	3	75	N.A.	15
13	G-R3-S1-e30	6	3	25	N.A.	30
14	G-R3-S2-e30	6	3	50	N.A.	30
15	G-R3-S3-e30	6	3	75	N.A.	30

* eccentricity ratio

2.2. Material Properties

All specimens were cast simultaneously using the same batch of ready-mix concrete. The concrete mix had a maximum aggregate size of 12.5 mm, a slump of 15 mm, and an average 28-day compressive strength of 32.5 ± 2.0 MPa, as determined from three standard cylinders tested according to ASTM C39/C39M [22] for every two specimens.

The GFRP bars and spirals used in the fabrication of the specimens were provided by Pultrall Inc. The longitudinal reinforcement consisted of #5 straight GFRP bars, while the transverse reinforcement was fabricated from #3 GFRP spirals, as the minimum acceptable size for spirals according to ACI CODE-440.11 [23]. Ties were made by cutting these spirals. To determine the mechanical properties of the GFRP bars, five tensile tests were conducted on coupons prepared in accordance with ASTM D7205/D7205M [24], and five compression tests were performed using a newly developed fixture and test method devised by the authors [25]. Material properties of the bent bars were supplied by the manufacturer. For steel-reinforced specimens, 15M bars were used as longitudinal reinforcement, while the ties were made from bent 10M bars. The material properties of the reinforcing bars are summarized in Table 2

Table 2 – Material properties of reinforcing bars

Material	Size	d_b (mm)	f_{ftu} (MPa)	f_{fcu} (MPa)	E_{ft} (GPa)	E_{fc} (GPa)	ε_{ftu} (-)	ε_{fcu} (-)
GFRP	#5	15.9	1020±25	952±66	53.7±0.1	50.0±0.7	0.021	0.018
	#3*	9.5	460	_	50	_	_	_
			f_y (MPa)		E_s (GPa)		ε_y (-)	
Steel**	15M	16.0	440		210		0.0021	
	10M	9.5	440		210		0.0021	

* Provided by the manufacturer.
** Tested by Khorramian et al. [26]

2.3. Specimen Preparation

The fabrication of GFRP reinforcement cages began by measuring and cutting the longitudinal and transverse reinforcement components according to the specified dimensions. Figure 1 illustrates the reinforcement detailing, which includes five general configurations for the transverse reinforcement along the column length and four configurations within the column cross-section. The longitudinal bars were fastened to the spirals using zip ties after being cut to size. The spirals were derived from larger spirals, and their pitch was set using block spacers to ensure evenly spaced, continuous transverse reinforcement. According to ACI CODE-440.11 [23], the clear spacing for the spirals was set to a minimum of 25 mm, a maximum of 75 mm, and an average value of 50 mm. Additionally, the 50 mm pitch was used as a fixed parameter in specimens G-R2-S2 and G-R4-S2, where the effect of varying longitudinal reinforcement ratios (2 and 4%) was the focus. To mitigate premature failure near the column ends, the spiral pitch was reduced to 25 mm over a length of 150 mm at both ends for the larger pitch values (50 and 75 mm).

For specimens with ties, the ties were cut from the spirals with the required length, considering overlap lengths of $20d_t$ and $28d_t$ (d_t is the nominal diameter of the transverse reinforcement) for G-R3-T2 and G-R3-T3, respectively. Two different tie spacings were used: a clear spacing of 75 mm to provide comparability with the largest spiral pitch, and a center-to-center spacing of 190 mm, which corresponds to the maximum allowable spacing [23]. The steel reinforcement was fabricated to be comparable to the GFRP reinforcement and designed in compliance with ACI 318 [27].

Strain gauges were installed on four longitudinal bars located at the corners of each specimen and on four points along the transverse reinforcement. This ensured eight strain gauges per specimen, providing redundancy for accurate strain measurement, with at least two gauges dedicated to each critical parameter. The strain gauges were then sealed with waterproof paste and wrapped with tape to prevent damage. Figure 2 presents the reinforcement cages. Once the reinforcement cages were assembled, they were placed into formworks, and concrete was poured after verifying the slump. Vibration was applied during concreting to ensure adequate compaction. The specimens were covered with wet burlap and plastic for the first 7 days to ensure proper initial curing, after which they were exposed to ambient conditions for the remainder of the curing period.

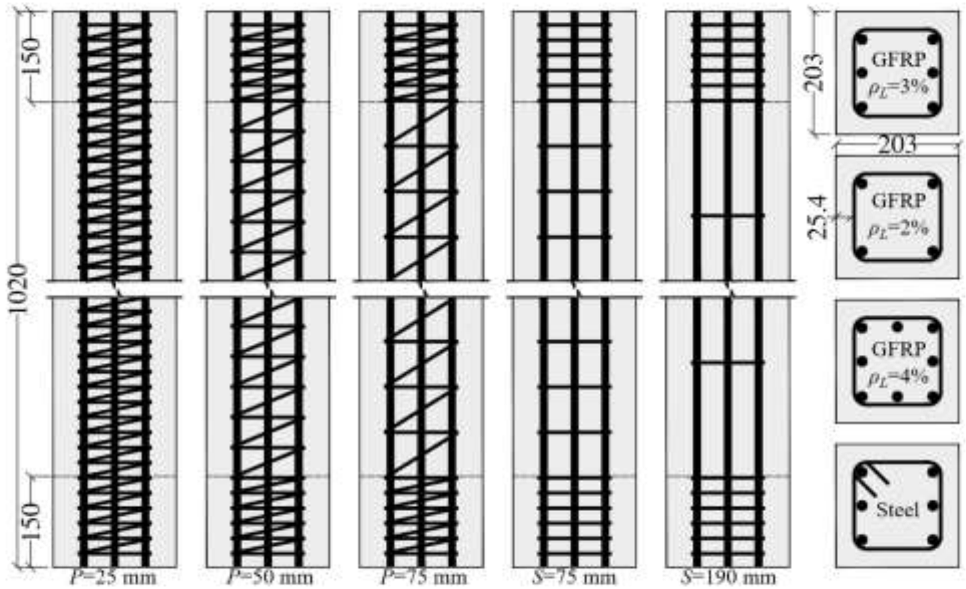

Figure 1 – Detail of the reinforcement for test specimens (All dimensions are in mm, *P*: Spiral pitch, and *S*: Tie spacing)

Figure 2 – Reinforcement cages for all specimens

2.4. Instrumentation and Test Setup

A horizontal axial loading setup was used in this study, as shown in Figure 3. The specimens were subjected to true axial compression, with load applied along their longitudinal axis. The horizontal setup was chosen to facilitate instrumentation while maintaining the same axial stress conditions as in a vertical test. The instrumentation used in the experiment included both internal and external components. Internally, strain gauges were installed on the reinforcement bars, with the gauge wires connected to a data acquisition system. Externally, the specimen was secured using end restraint fixtures, consisting of steel collars attached to both ends of the specimen, which provided pin supports. To prevent stress concentration at the fixture edges, thin grout bags were placed between the steel fixtures and the specimen, and the fixtures were tightened with four bolts.

One end of the specimen was fixed to a reaction block, while the other was connected to the displacement transfer guide of the 2 MN hydraulic actuator. The alignment of the specimen was verified using laser point levels after initial tape measurements. String potentiometers (SP) were attached to pedestals on either side of the specimen, with their strings connected to the mid-height of the specimen to measure lateral displacement. Additionally, a linear potentiometer (LP) was installed at mid-height as a backup to monitor lateral displacement, particularly for eccentric loading conditions. All measurements, including strain and displacement, were continuously recorded through the data acquisition system, while load application was controlled via the hydraulic actuator.

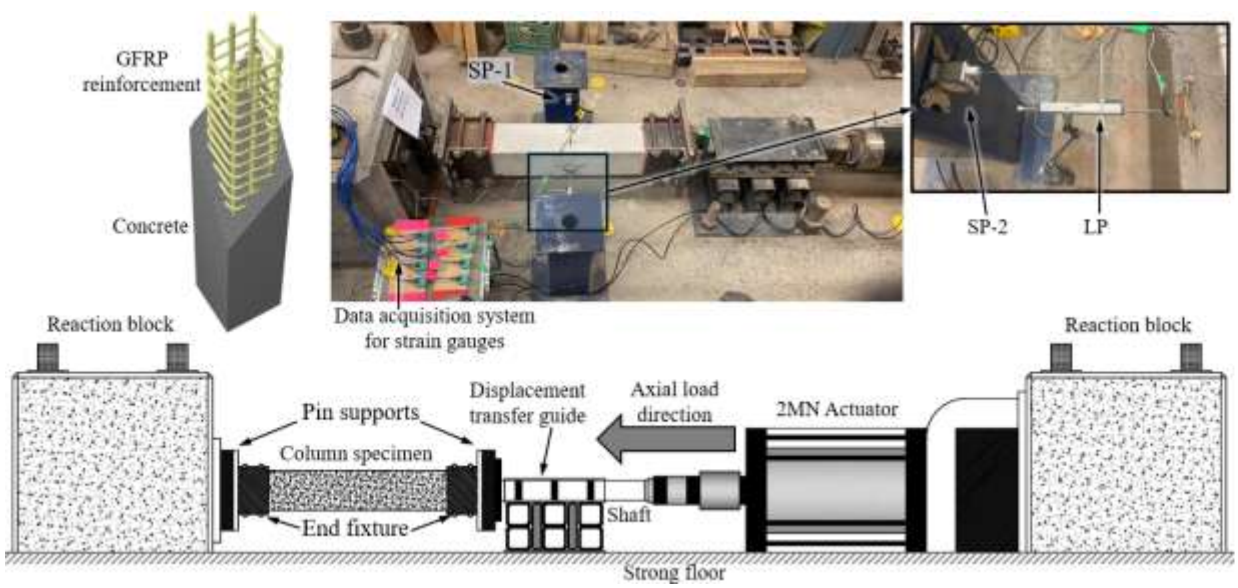

Figure 3 – Test setup and external instrumentation

2.5. Test Procedure

The specimens were subjected to both concentric and eccentric loading, with the eccentricity determined by the placement of the end pin on the supports. The tests were conducted using a displacement-controlled method at a loading rate of 2.0 mm/min, applied through a 2 MN MTS machine which was equipped with a high-precision servo-controlled hydraulic actuator, which automatically adjusted to maintain the prescribed displacement rate, even in cases of stiffness degradation. Prior to the main loading, a small preloading was applied to eliminate any minor voids in the load transfer system. The applied load was recorded using the internal load cell of the hydraulic actuator, while both the load and displacement data were simultaneously transmitted to the data acquisition system. The loading process continued until either a sudden failure occurred, indicated by an abrupt drop in load, or until the load decreased to less than 20% of the peak value. This approach ensured that all failure modes and their sequences were captured during the tests.

3. EXPERIMENTAL RESULTS AND DISCUSSION

3.1. Failure Mechanisms

3.1.1. Behavior under Concentric Load

Figure 4 compares the failure modes for the specimens with various spiral pitches. G1-R3-S1-e0 exhibited gradual longitudinal crack growth on one side following spalling of the concrete cover at peak load. This cracking occurred on the compression side, influenced by the internal load distribution within the column, which was affected by the spiral configuration. After the initial load drop, the column maintained a plateau load of approximately 1200 kN, with intermittent audible sounds from the GFRP reinforcement as displacement increased. Extensive cover spalling occurred along almost the entire column length, followed by a sudden crushing of the longitudinal bars at mid-height, resulting in a sharp drop of load.

For G1-R3-S2-e0, concrete cracking was observed around the peak load, followed by visible crack growth on one side and the spalling of large chunks of the concrete cover. Longitudinal cracks developed along the length of the column. After reaching a plateau load, the column failed as the longitudinal bars slipped into the end grout bag on the actuator side rather than crushing. This may have been due to the use of a thicker grout bag in this test. Consequently, the peak load recorded for this specimen was lower than that of G1-R3-S3-e0, which had a larger pitch.

In G1-R3-S3-e0 with the largest spiral pitch, cracks initiated locally at mid-height, with the concrete cover cracking around the peak load. However, the load drop following the peak was more sudden and pronounced, without causing damage to the GFRP bars. After that, the column experienced increased deformation and a further load reduction, ultimately failing due to the sudden crushing of the longitudinal bars.

Figure 4 – Comparing the failure modes in columns with different spiral pitches

Figure 5 illustrates the failure modes in column specimens with different tie configurations and materials. G1-R3-T1-e0, featuring ties spaced at 75 mm intervals with a $20d_t$ overlap, exhibited gradual, calm cracking at the peak load, with cracks initiating and expanding longitudinally around mid-height. The load plateau persisted for a relatively long duration. The final failure was explosive, with the concrete cover forcefully ejecting. The column ultimately failed due to tie opening at the zip tie connection, followed by buckling and crushing of the longitudinal bars.

G1-R3-T2-e0 was manufactured with the same tie overlap as G1-R3-T1-e0, but with a larger tie spacing of 190 mm (2.5 times the spacing in G1-R3-T1-e0). Prior to reaching the peak load, cracking sounds were heard, likely from the concrete cover due to the expansion of the GFRP ties. Upon reaching the peak load, the specimen failed abruptly with a loud noise, resulting in the simultaneous burst of both the concrete cover and core. The larger tie spacing in this specimen was insufficient to contain the concrete core, and the tie overlap was inadequate to prevent tie opening and consequently buckling and shear crippling of the longitudinal bars.

In G1-R3-T3-e0, the same transverse reinforcement pattern was used as in G1-R3-T2-e0, with the key difference being an increase in tie overlap, incorporating 90^{o} hooks, from $20d_t$ to $28d_t$. This adjustment resulted in a higher peak load, and a more ductile failure compared to G1-R3-T2-e0. At peak load, the concrete cover cracked, followed by crack propagation and spalling around mid-height. After a load drop of approximately 30%, the column ultimately failed due to the crushing of the longitudinal bars, with no observed tie opening or failure. This underscores the critical importance of tie fastening and overlap in influencing the failure mode of the column.

To enable a comparison between the behavior of steel-RC and GFRP-RC columns, S1-R3-T2-e0 was tested with the same reinforcement configuration as G1-R3-T2-e0 and G1-R3-T3-e0. The primary difference, aside from the reinforcement material, was that the ties in S1-R3-T2-e0 had 135^{o} hooks, whereas the GFRP-RC specimens used 90^{o} hooks. Test observations indicated that S1-R3-T2-e0 sustained load without visible cracking until it reached peak load. Only a few seconds before failure, faint sounds of concrete cracking were heard, followed by a sudden failure characterized by buckling of the longitudinal bars between the ties, with no damage to the ties, as shown in the figure below. Comparing the behavior of this specimen with the two GFRP-RC counterparts revealed that all columns failed due to longitudinal bar buckling—after yielding of the steel reinforcement in S1-R3-T2-e0, and due to lateral deformation in the GFRP bars in the other specimens. The tie opening in G1-R3-T2-e0 led to a more sudden failure at peak load.

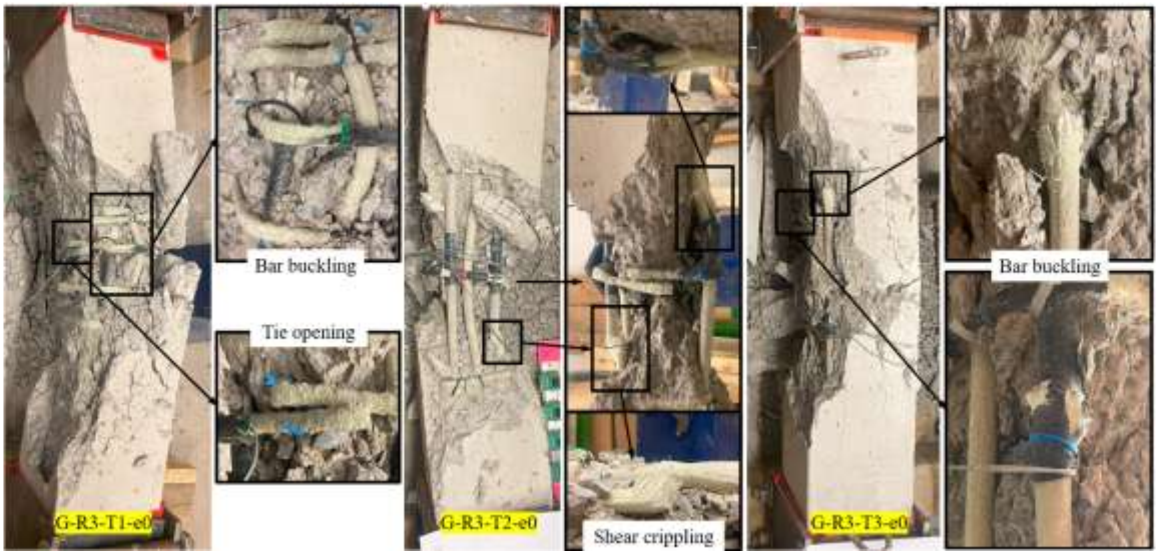

(a)

(b)

Figure 5 – Comparing failure modes in columns with different tie configurations and materials: a) GFRP-RC columns, b) Steel-RC columns

To investigate the effect of longitudinal reinforcement ratio, ρ_L, G1-R2-S2-e0 and G1-R4-S2-e0 were manufactured with a ρ_L of 2% and 4%, respectively, and a spiral pitch of 50 mm, for comparison with G1-R3-S2-e0, in which ρ_L=3% with the same spiral pitch. The failure modes are illustrated in Figure 6.

In G1-R2-S2-e0, cracks appeared around the concrete cover near peak load, primarily concentrated around mid-height. As the load began to drop, the cracks propagated longitudinally along the column, eventually leading to failure through the crushing of the longitudinal bars. G1-R2-S2-e0 exhibited less ductility compared to G1-R3-S2-e0, due to the lower number of longitudinal bars and consequently reduced confinement effect.

G1-R4-S2-e0 exhibited initial cracking around peak load, primarily at mid-height, with longitudinal cracks propagating along the column. After a 13% drop in strength, the confinement effects became evident, as the load began to increase again. The concrete core maintained its integrity despite widespread cracking in the cover. This recovery continued, and a second peak load, approximately 97% of the first peak, was reached. Around the second peak, continuous sound of GFRP damage was detected. Immediately following this second peak, the specimen failed rapidly, with the longitudinal bars crushing one after another in less than a second, as shown in Figure 6.

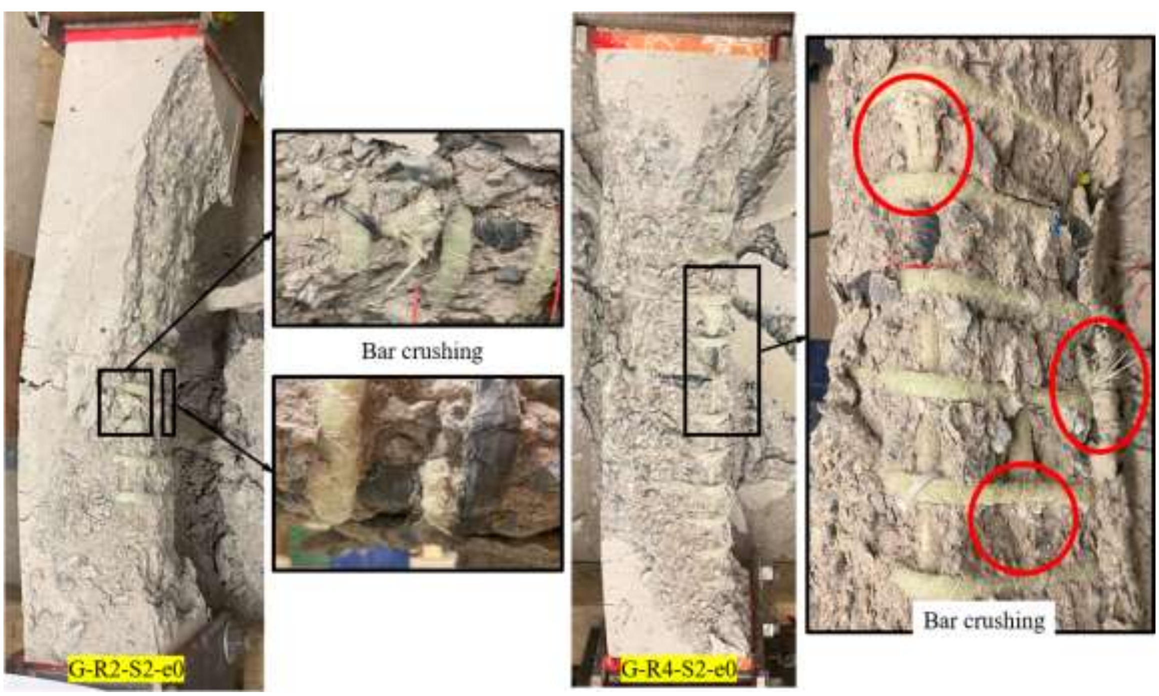

Figure 6 – Comparing the effect of longitudinal bar reinforcement used with square spirals

3.1.2. Behavior under Eccentric Load

G1-R3-S1-e15, G1-R3-S2-e15, and G1-R3-S3-e15 were tested under 15% eccentricity, with spiral pitches of 25, 50, and 75 mm, respectively. The failure modes are illustrated in Figure 7. G1-R3-S1-e15 exhibited cracks around mid-height at peak load, which propagated toward the column ends. The specimen maintained about 60% of the peak load for around 18 mm axial stroke displacement before ultimately failing due to slipping of the longitudinal bars in the concrete. The small spiral pitch effectively restrained the bars from buckling, and the bars released energy by slipping from one end on the tensile side. However, if bars were anchored at the ends, the failure mode would possibly change into crushing of the compression bars like G1-R3-S1-e0.

G1-R3-S2-e15, with a 50 mm spiral pitch, demonstrated slightly different post-peak behavior. Cracks initiated at peak load around mid-height and spread toward the ends, though the cover spalling was more localized compared to G1-R3-S1-e15. After approximately 15 mm of axial displacement beyond the peak load, the specimen failed due to crushing of the longitudinal bars on the compression side. The test continued, and after about 10 mm of additional displacement, the spiral ruptured at two locations, as shown in Figure 7.

G1-R3-S3-e15, with a 75 mm spiral pitch, developed cracks more abruptly at peak load, accompanied by cover spalling. After the load dropped to less than 50% of the peak load, it continued to decrease gradually. At around 8 mm of axial stroke displacement, the specimen failed due to crushing and fiber splitting of the longitudinal bars on the compression side, producing a loud noise. Further displacement caused the spiral to rupture.

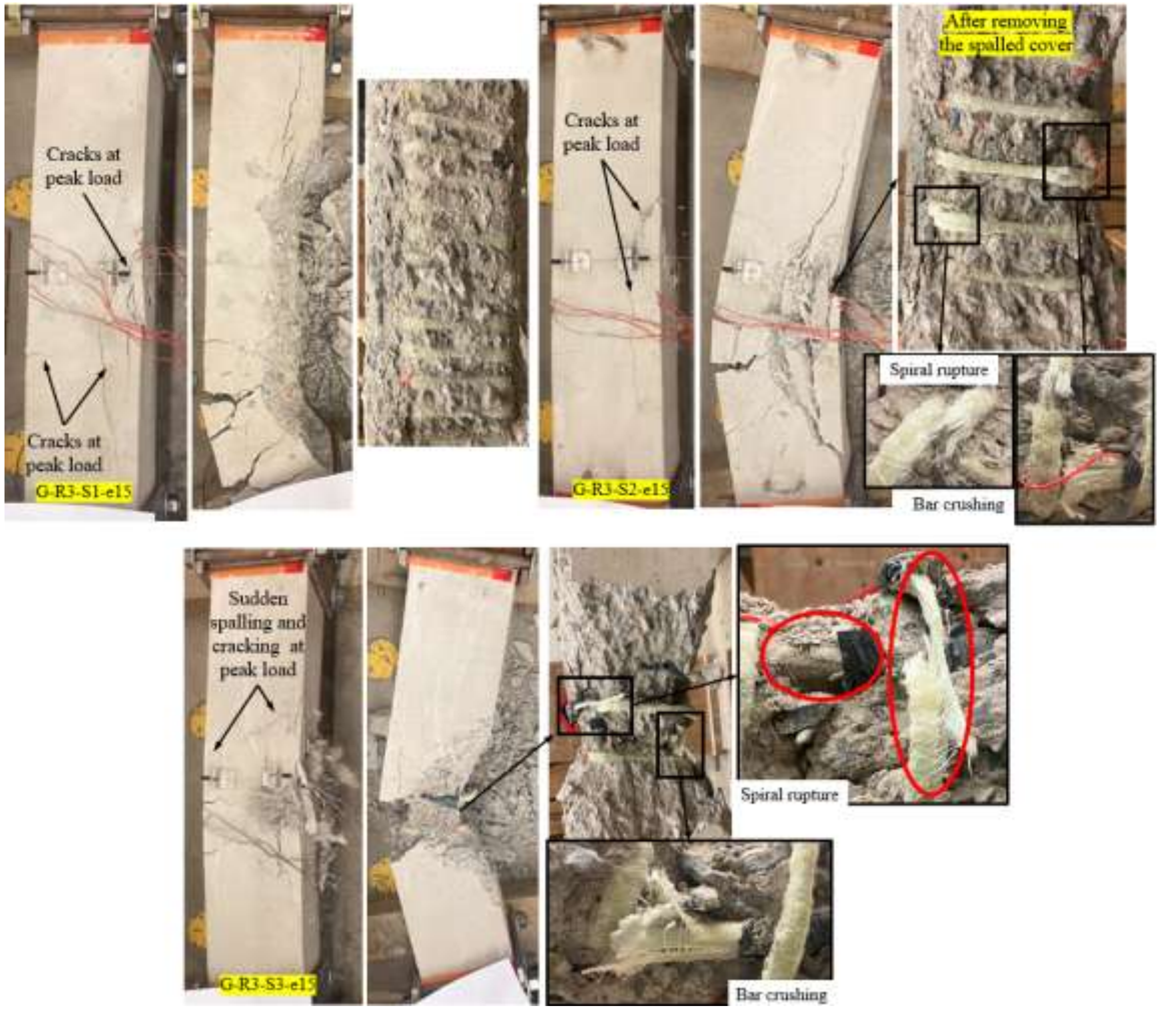

Figure 7 – Comparing the failure modes in columns with different spiral pitches under 15% load eccentricity

G1-R3-S1-e30, G1-R3-S2-e30, G1-R3-S3-e30 were tested under 30% load eccentricity, with varying spiral pitches of 25, 50, and 75 mm, respectively. Figure 8 compares the failure patterns in these three specimens. In G1-R3-S1-e30, the load increased until reaching the peak load, with cracks forming on both the compression and tension sides. Compressive cracks appeared around mid-height, extending longitudinally along the column, while tensile cracks developed transversely near the loading end fixture. As shown in Figure 8, the concrete cover on the compression side fully spalled, and the load dropped to less than 20% of the peak load. No crushing of the longitudinal bars or spiral failure was observed. However, some bars on the tension side slipped through the concrete at high axial displacements, which became visible after removing the end fixtures.

G1-R3-S2-e30 displayed behavior similar to G1-R3-S1-e30, with compressive cracks initiating at mid-height and transverse tensile cracks forming near the loading end fixture. However, the tensile cracks in this specimen were located farther from the end fixture than in G1-R3-S1-e30. The test concluded in a similar manner, with the load dropping to less than 20% of the peak load and no reinforcement failure. Bars on the tension side slipped through the concrete during the very final stages of loading at high axial displacements.

G1-R3-S3-e30, with a 75 mm spiral pitch, exhibited slightly different behavior. While compressive cracks still initiated around mid-height, they did not propagate as far toward the ends as in the other two specimens. Additionally, tensile cracks were observed around mid-height rather than near the end fixture. This variation is likely due to the larger spiral pitch, which made the specimen more susceptible to concentrated damage around mid-height. After the peak load, the load decreased but remained stable through larger deformations until the longitudinal bars on the compressive side of the column ultimately failed by crushing.

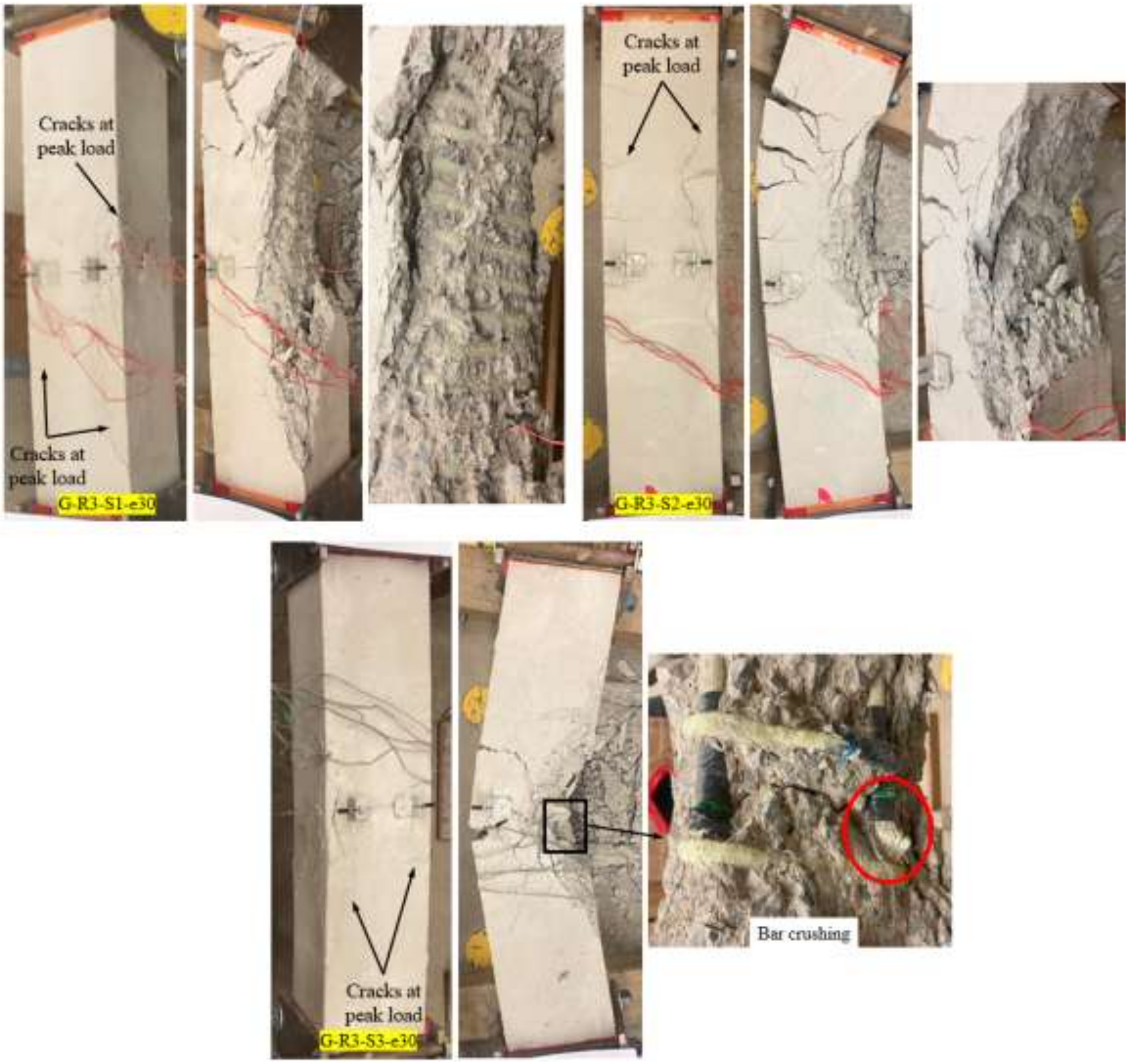

Figure 8 – Comparing the failure modes in columns with different spiral pitches under 30% load eccentricity

3.1.3. Analysis of Failure Observations

As summarized in Table 3, under concentric loading, the effect of spiral pitch was evident in the failure modes and post-peak behavior. Specimens with a small spiral pitch of 25 mm (G1-R3-S1-e0) exhibited a gradual failure progression with significant post-peak load retention, as the closely spaced spirals effectively confined the core and restrained bar buckling. In contrast, increasing the spiral pitch to 50 mm (G1-R3-S2-e0) resulted in slightly weaker confinement, leading to bar slip. The specimen with the largest spiral pitch of 75 mm (G1-R3-S3-e0) demonstrated brittle failure, with sudden bar crushing and a steep post-peak load drop due to inadequate confinement. The role of tie spacing and overlap was also significant, as seen in the T1, T2, and T3 specimens. The smallest tie spacing (T1, 75 mm with $20d_t$ overlap) provided some confinement, though ties opened at the zip tie connection, contributing to progressive failure. Increasing the tie spacing to 190 mm (T2) with the same overlap resulted in an even more abrupt failure due to insufficient confinement, as ties were unable to prevent bar buckling. However, when the overlap was increased to $28d_t$ (T3), the failure became more ductile, with improved confinement delaying bar crushing. Comparing steel and GFRP ties, the steel-reinforced specimen (S1-R3-T2-e0) exhibited no tie failure, but bar buckling after yielding resulted in sudden collapse. The influence of the longitudinal reinforcement ratio was also observed; a lower ratio of 2% (G1-R2-S2-e0) led to brittle failure due to reduced confinement, whereas a higher ratio of 4% (G1-R4-S2-e0) improved structural integrity, allowing for a secondary peak load before final failure.

Table 3 – Summary of the failure modes observed under concentric loading

Specimen ID	Concrete Cover Behavior	Longitudinal Bars Failure Mode	Spiral/Tie Effect	Overall Behavior
G1-R3-S1-e0	Extensive spalling, longitudinal cracks	Sudden crushing at mid-height	Confined core but progressive failure	Gradual failure, load plateau, bar crushing
G1-R3-S2-e0	Large spalling, longitudinal cracks	Bar slip into grout bag instead of crushing	Spiral confinement, but bar slip affected failure	Gradual failure, load plateau, bar slip
G1-R3-S3-e0	Local cracking at mid-height, sudden spalling	Sudden bar crushing	Largest spiral pitch, weaker confinement	Brittle failure, load drop after peak
G1-R3-T1-e0	Gradual cracking, explosive spalling	Buckling and crushing	Ties opened at zip tie connection	Progressive failure, then sudden failure
G1-R3-T2-e0	Sudden burst of cover and core	Bar buckling due to tie opening	Large tie spacing, inadequate overlap	Abrupt failure at peak load
G1-R3-T3-e0	Cover cracking and spalling	Crushing after load drop	Improved tie overlap, no tie opening	More ductile failure, delayed bar crushing
S1-R3-T2-e0	No visible cracking until failure	Buckling after yielding	Steel ties (135° hooks) prevented tie failure	Sudden bar buckling failure, no tie damage
G1-R2-S2-e0	Cover cracks at mid-height, longitudinal cracking	Bar crushing	Lower confinement due to fewer bars	Less ductile, brittle failure
G1-R4-S2-e0	Initial cracking, second peak load observed	Progressive bar crushing	Strong confinement, maintained integrity	Higher ductility, strength recovery before final failure

For specimens subjected to eccentric loading, as shown in Table 4, failure patterns and post-peak behavior were significantly influenced by both spiral pitch and load eccentricity. In the 15% eccentricity series, all specimens developed mid-height cracks at peak load, with variations in failure modes based on confinement efficiency. The smallest pitch (G1-R3-S1-e15, 25 mm) provided strong confinement, preventing bar buckling and allowing the specimen to retain about 60% of the peak load over an 18 mm axial displacement before final failure due to bar slip on the tensile side. The medium pitch specimen (G1-R3-S2-e15, 50 mm) exhibited slightly weaker confinement, leading to localized cover spalling and bar crushing on the compression side. The failure was more sudden compared to G1-R3-S1-e15, and at larger displacements, the spiral ruptured at two locations. In the specimen with the largest spiral pitch (G1-R3-S3-e15, 75 mm), failure was more abrupt, with significant cover spalling and fiber splitting in the longitudinal bars on the compression side. The failure occurred earlier, with a loud noise indicating brittle crushing of the bars, and further displacement led to spiral rupture. The influence of spiral pitch on failure modes became even more pronounced in the 30% eccentricity series. Specimens with smaller pitches (G1-R3-S1-e30 and G1-R3-S2-e30) exhibited extensive cracking on both the compression and tension sides. Compressive cracks formed at mid-height, while tensile cracks developed near the loading end fixture. The concrete cover fully spalled on the compression side, causing a substantial post-peak load drop. Unlike in the e15 series, no crushing of longitudinal bars or spiral rupture was observed; instead, bars on the tension side slipped through the concrete at large axial displacements. In G1-R3-S3-e30 (75 mm pitch), the crack pattern differed, as tensile cracks formed around mid-height rather than near the loading fixture, likely due to the weaker confinement provided by the larger spiral pitch. The post-peak load reduction was more gradual, but the ultimate failure was concentrated at mid-height, where the longitudinal bars in compression failed by crushing.

Table 4 – Summary of the failure modes observed under eccentric loading

Specimen ID	Concrete Cover Behavior	Longitudinal Bars Failure Mode	Spiral Effect	Overall Behavior
G1-R3-S1-e15	Cracks at mid-height, propagated toward ends	Bar slip on tensile side	Small spiral pitch prevented buckling	Gradual failure, high post-peak load retention
G1-R3-S2-e15	Mid-height cracking, localized cover spalling	Crushing on compression side, delayed spiral rupture	Moderate spiral pitch provided partial confinement	More sudden failure, spiral rupture at large displacement
G1-R3-S3-e15	Abrupt cracking, significant cover spalling	Crushing and fiber splitting on compression side	Largest pitch led to concentrated failure	Brittle failure, sudden bar and spiral rupture
G1-R3-S1-e30	Cracks on both compression and tension sides, full spalling on compression side	No crushing, but bars slipped through concrete	Strong confinement, but tensile bars slipped	High ductility, significant post-peak deformation
G1-R3-S2-e30	Mid-height compressive cracks, transverse tensile cracks farther from fixture	No crushing, bars slipped at high displacement	Similar to S1-e30, but tensile cracks formed differently	Ductile failure, bars slipped instead of crushing
G1-R3-S3-e30	Mid-height compressive and tensile cracks, less crack propagation	Crushing of bars on compression side	Larger spiral pitch led to localized damage	More concentrated failure at mid-height, stable post-peak behavior

Comparing concentric and eccentric loading results, a key distinction was the distribution of damage and failure modes. Under concentric loading, failure was more uniform, with clear confinement effects from spirals delaying bar crushing and influencing post-peak behavior. In eccentric loading, specimens exhibited asymmetric damage, with compression-side failure in higher eccentricity cases. Smaller spiral pitches generally improved confinement, delaying failure and increasing post-peak load retention, while larger spiral pitches resulted in more localized failures and sudden collapses. The slip of longitudinal bars in tension was observed in several eccentric loading cases, highlighting the importance of anchorage and confinement effectiveness in GFRP-reinforced columns.

3.2. Quantitative test results

Tables 5 and 6 present quantitative results for specimens tested under concentric and eccentric loading, respectively. In Table 5, the steel-reinforced specimen (S1-R3-T2-e0) achieved the highest peak load, with longitudinal reinforcement contributing approximately 30% of the total load capacity. For GFRP-RC columns, specimens with tighter spiral pitches (e.g., G1-R3-S1-e0) or higher longitudinal reinforcement ratios (e.g., G1-R4-S2-e0) demonstrated increased peak load values. Overall, GFRP specimens showed a reinforcement contribution between 7% and 15%, influenced by the ratio of longitudinal bars and spirals, though with minimal sensitivity to tie configuration. Increasing the spiral pitch from 25 mm to 75 mm led to a approximately 6% reduction in peak load for spiral-reinforced specimens. This decrease is attributed to reduced confinement, which diminished the contribution of the concrete core to load resistance while increasing reliance on the longitudinal bars. Comparatively, Abdelazim et al. [28] observed only a 1% reduction in the load-bearing capacity of concentrically loaded circular columns when the spiral pitch increased from 40 mm to 80 mm. This suggests that square spirals are more sensitive to pitch variations than circular spirals, potentially due to the stress concentration at the corners, which may result in less uniform confinement. In circular spirals, the confinement effect is more evenly distributed, making pitch variation less impactful.

Specimen G1-R3-T3-e0, with a tie overlap of $28d_t$ and a spacing of $12d_b$, exhibited higher peak loads than specimens with a $20d_t$ overlap and spacings of $5d_b$ and $12d_b$. This suggests that increasing the overlap length enhances tie effectiveness in restraining lateral expansion, leading to improved confinement and load-bearing capacity. However, Hadhood et al. [29] observed that increasing hoop overlap from $20d_t$ to $60d_t$ in circular columns had a negligible effect on peak load (3% increase), with no evidence of slippage in the $20d_t$-overlapped hoops. This indicates that, for circular hoops, a $20d_t$ overlap may be sufficient to maintain load transfer efficiency. In contrast, the present study suggests that square ties require a greater overlap length and hooked anchorage to achieve similar confinement efficiency, likely due to differences in stress distribution and the engagement of ties at the corners. This highlights a potential limitation of current tie design approaches for GFRP-reinforced square columns, which may require further optimization to enhance confinement effectiveness.

Compressive strains in GFRP bars remained consistent across configurations, while the steel-reinforced specimen exhibited slightly lower strain values despite its higher load capacity, suggesting enhanced load transfer efficiency. Tensile strains in ties were generally higher than those in spirals across GFRP specimens; however, in specimen G1-R3-T3-e0, the increased overlap length in ties resulted in reduced deformation near the peak load, indicating improved confinement.

Table 6 outlines the effects of eccentric loading on load capacity, moment capacity, and lateral deformation in GFRP-RC columns. Peak load values decreased with increasing eccentricity due to the combined effects of axial load and bending moment. However, for a given eccentricity, the peak loads remained nearly consistent across specimens with varying spiral pitches, indicating that the square spiral provided negligible confinement under eccentric loading. Specifically, under 15% and 30% eccentricity, the peak load was approximately 60% and 40% of that under concentric loading, respectively. This aligns with findings by Abdelazim et al. [28], who reported that the peak load of circular columns under 66% eccentricity dropped to just 11% of their concentric capacity, with minimal influence from spiral pitch variations (80 mm vs. 40 mm). The greater strength retention in square columns at 30% eccentricity compared to Abdelazim et al.'s circular columns at 66% eccentricity suggests that the load redistribution mechanisms may differ between square and circular spirals. This could be due to differences in the confinement efficiency or load transfer patterns between square and circular reinforcement configurations.

Specimens with 30% eccentricity demonstrated higher moment capacity due to larger lateral displacements, which contributed to increased bending moments despite the reduction in peak axial load. Compressive strain in the longitudinal bars at peak load remained relatively stable across eccentricity levels. Spiral strain at peak load increased when the pitch was raised from 25 mm to 50 mm but decreased at 75 mm, suggesting that a 75 mm pitch may be approaching an optimal design in terms of confinement efficiency and deformation compatibility. Lateral deformations showed a minimal increase with larger spiral pitches under eccentric loading conditions.

Table 5 – Results under concentric loading

Specimen ID	P_{max} (kN)	$\varepsilon_{fc,0}$ (-)*	$\varepsilon_{st,0}$ (-)*	P_R (kN)*	P_R/P_{max}
G1-R3-S1-e0	1489	-0.0026	0.0002	152	0.10
G1-R3-S2-e0	1384	-0.0025	0.0003	151	0.11
G1-R3-S3-e0	1396	-0.0030	0.0003	177	0.13
G1-R3-T1-e0	1455	-0.0029	0.0010	172	0.12
G1-R3-T2-e0	1317	-0.0027	0.0012	160	0.12
G1-R3-T3-e0	1472	-0.0027	0.0007	162	0.11
G1-R2-S2-e0	1441	-0.0027	0.0005	107	0.07
G1-R4-S2-e0	1461	-0.0027	0.0004	218	0.15
S1-R3-T2-e0	1612	-0.0024	0.0002	480	0.30

* Measured at P_{max}

$\varepsilon_{fc,0}$: Compressive strain in bars

$\varepsilon_{st,0}$: Tensile strain in spirals and ties

Table 6 – Results under eccentric loading

Specimen ID	P_{max} (kN)	$\varepsilon_{fc,0}$ (-)*	$\varepsilon_{ft,0}$ (-)*	$\varepsilon_{st,0}$ (-)*	δ (mm)*	M_{max} (kN-m)*
G1-R3-S1-e15	875	-0.0029	0.0005	0.0004	4.4	31.6
G1-R3-S2-e15	865	-0.0032	-0.00002	0.0007	5.5	32.2
G1-R3-S3-e15	869	-0.0032	-0.0007	0.0005	5.7	32.5
G1-R3-S1-e30	537	-0.0025	0.0025	0.0003	8.8	38.8
G1-R3-S2-e30	558	-0.0018	0.0018	0.0006	9.6	40.8
G1-R3-S3-e30	553	-0.0022	0.0020	0.0004	8.4	39.7

* Measured at P_{max}

$\varepsilon_{fc,0}$: Strain in bars on the compression side

$\varepsilon_{ft,0}$: Strain in bars on the tension side

$\varepsilon_{st,0}$: Tensile strain in spirals

δ: Mid-height lateral displacement

3.2.1. Axial Load-displacement

The load vs. axial stroke displacement curves for all concentric tests are presented in Figure 9. The horizontal dashed line represents the load corresponding to the average concrete strength (f'_c) from standard cylinder tests, which has been multiplied by the column's cross-sectional area (A_g) to obtain the theoretical maximum load the plane concrete section could sustain. To assess the effect of longitudinal reinforcement ratios, the performance of specimens G1-R2-S2-e0, G1-R3-S2-e0, and G1-R4-S2-e0, with 2%, 3%, and 4% longitudinal reinforcement ratios, respectively, are compared. It is observed that increasing the longitudinal reinforcement ratio from 2% to 4% results in only a marginal increase in peak load, approximately 1.5%. This suggests that the contribution of additional longitudinal reinforcement to peak strength is minimal. The slightly lower peak load in G1-R3-S2-e0 compared to G1-R2-S2-e0 can be attributed to bar slippage, which was observed during testing. However, increasing the amount of longitudinal reinforcement positively influenced the confinement of the concrete core, significantly improving post-peak behavior. In particular, G1-R4-S2-e0, with the highest reinforcement ratio, exhibited a secondary peak load reaching approximately 98% of the initial peak load, indicating enhanced deformability due to the denser reinforcement cage around the concrete core.

The pitch of the spirals also plays a significant role in the post-peak behavior of the columns. When the spiral pitch increased from 25 mm (G1-R3-S1-e0) to 75 mm (G1-R3-S3-e0), the failure mode shifted from a more ductile response to a more abrupt loss of load-bearing capacity. For example, after reaching its peak load, G1-R3-S1-e0 experienced a gradual load reduction to approximately 90% of its peak load, and then to 85%, while maintaining load-bearing capacity for about 10 mm of axial displacement. In contrast, G1-R3-S2-e0, with a 50 mm spiral pitch, exhibited a similar initial load drop of around 15%, but the ability to sustain the load over the axial displacement was shorter. Finally, G1-R3-S3-e0, with the largest spiral pitch of 75 mm, showed the most brittle behavior, with a sharp drop after peak load, indicating insufficient confinement.

When comparing the performance of columns with square ties versus those with square spirals, G1-R3-T1-e0, which utilized ties with a 75 mm spacing, exhibited brittle behavior like G1-R3-S3-e0, which used square spirals with the same spacing. However, differences in tie spacing and overlap configuration significantly affect performance. Specimens G1-R3-T2-e0 and G1-R3-T3-e0, both with 190 mm tie spacing, showed brittle failure with a sudden drop after the peak load, in contrast to G1-R3-T1-e0, which had a 75 mm tie spacing and demonstrated a more gradual post-peak decline. The lower peak load observed for G1-R3-T2-e0 is due to the sudden failure triggered by tie opening, a consequence of insufficient overlap ($20d_t$), which led to a rapid loss of confinement and the premature detonation of the concrete cover before the column reached its maximum strength. This failure mode was mitigated in G1-R3-T3-e0, where a larger tie overlap of $28d_t$ was employed, resulting in improved confinement and a higher peak load than G1-R3-T1-e0. Nevertheless, G1-R3-T3-e0 still experienced a sharp post-peak load drop, primarily due to the large tie spacing, which allowed longitudinal bars to buckle.

Finally, the steel-reinforced specimen, S1-R3-T2-e0, which uses steel instead of GFRP bars with a 3% longitudinal reinforcement ratio and square ties at 190 mm spacing with a $20d_t$ overlap, achieved the highest peak load among all specimens. The peak load for S1-R3-T2-e0 was approximately 10% higher than that of its GFRP-RC counterpart, G1-R3-T3. However, both specimens exhibited sudden failure characterized by a sharp drop in load after the peak. This behavior can be attributed to the buckling of the longitudinal bars, which was triggered by the large tie spacing and the reduced confinement it provided.

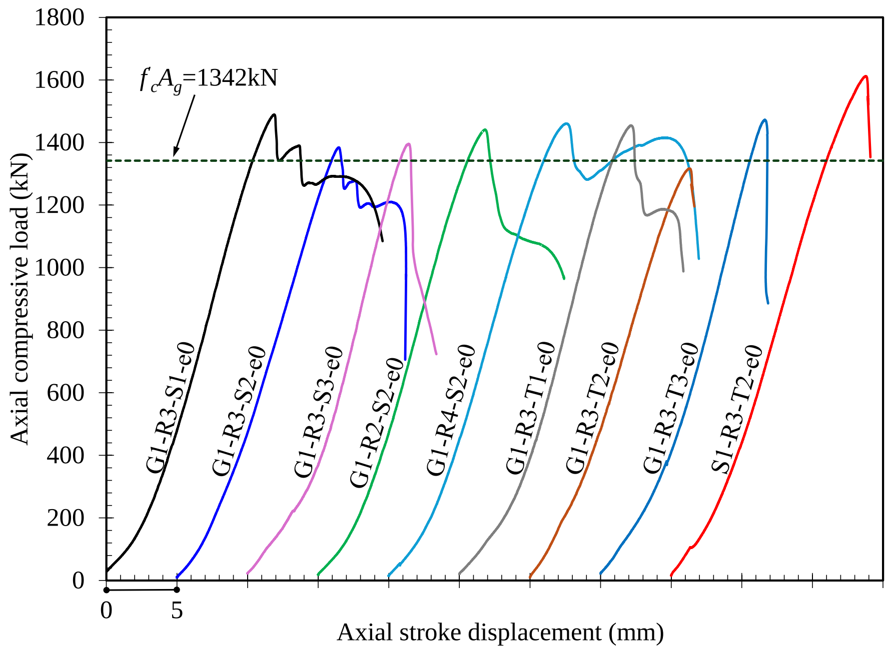

Figure 9 – Load versus axial stroke displacement of specimens under concentric load

Figure 10 illustrates the impact of spiral pitch and eccentricity on the overall performance of the columns in terms of load-carrying capacity and post-peak behavior. Regarding the post-peak behavior, columns with lower spiral pitch exhibited a smaller load drop and sustained the load for a longer duration after the initial peak. This indicates that tighter spirals provide better confinement and help the column maintain its structural integrity for a longer period after reaching peak load. However, as eccentricity increases, the failure point of the longitudinal bars becomes more aligned across specimens with different spiral pitches. This convergence in behavior can be attributed to the reduced effectiveness of confinement as the eccentricity grows. With greater eccentricity, the bending effects dominate, reducing the influence of spiral confinement, and thus making the behavior of columns with different pitches more similar under the same load eccentricity.

With respect to peak load, it is seen that as eccentricity increases, the peak load of the specimens with the smallest spiral pitch becomes slightly lower than that of specimens with larger spiral pitches. This trend can be attributed to the diminishing effectiveness of confinement as eccentricity increases. Additionally, at higher eccentricities, particularly at 30%, a smaller spiral pitch means the presence of more spiral reinforcement, which may increase the likelihood of cover separation from the core due to bending effects on the section. This explains why, at 30% eccentricity, the peak load of G1-R3-S1-e30 is slightly lower than that of G1-R3-S2-e30 and G1-R3-S3-e30.

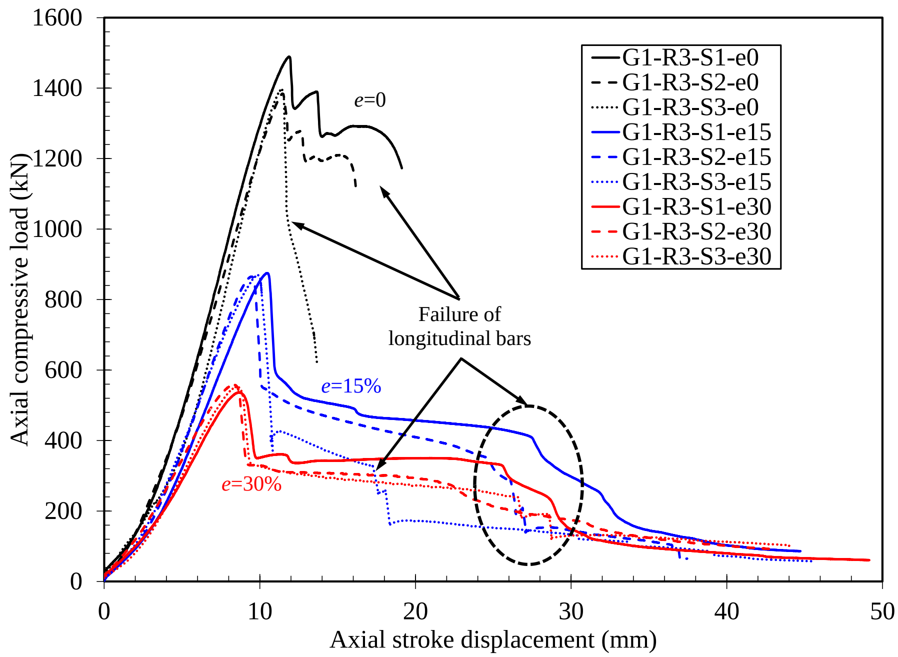

Figure 10 – Load versus axial stroke displacement of specimens under eccentric load

3.2.2. Lateral displacement

According to Figure 11 the behavior of the specimens under each eccentricity ratio is very similar up to the peak load, with the peak loads being almost identical. However, the smaller spiral pitch provided greater stability after the peak, as the load resistance remained slightly higher. The lateral deformation at which the longitudinal reinforcement failed was approximately the same across all specimens. However, G1-R3-S3-e15, with a larger spiral pitch, exhibited a sudden drop after the peak load and experienced earlier crushing of the longitudinal bars compared to the other specimens under low eccentricity.

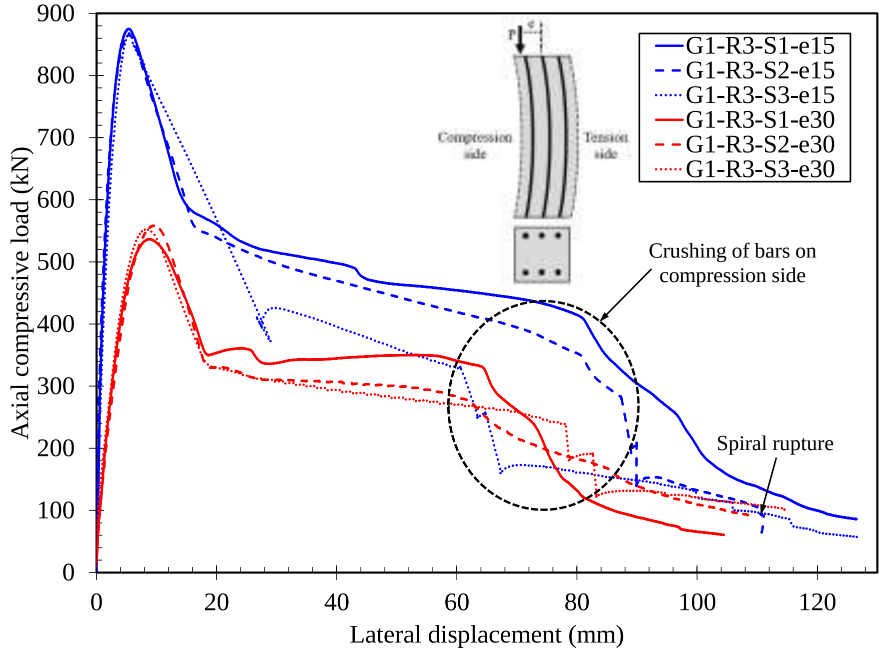

Figure 11 – Load versus lateral displacement of specimens under eccentric load

3.2.3. Longitudinal Reinforcement Strain

Figure 12 illustrates the load versus average strains in the longitudinal bars of specimens under concentric loading. The threshold f'_cA_g shows the theoretical maximum load the plane concrete section could sustain. As seen, the specimens exhibited similar behavior in the ascending portion of the diagrams, regardless of reinforcement pattern, up to approximately $0.85f'_cA_g$. However, the steel-reinforced specimen remains linear-elastic longer, up to the point where the longitudinal bars yield, after which it experienced failure following a load decrease. In contrast, GFRP-RC specimens display nonlinearity just before reaching the peak load.

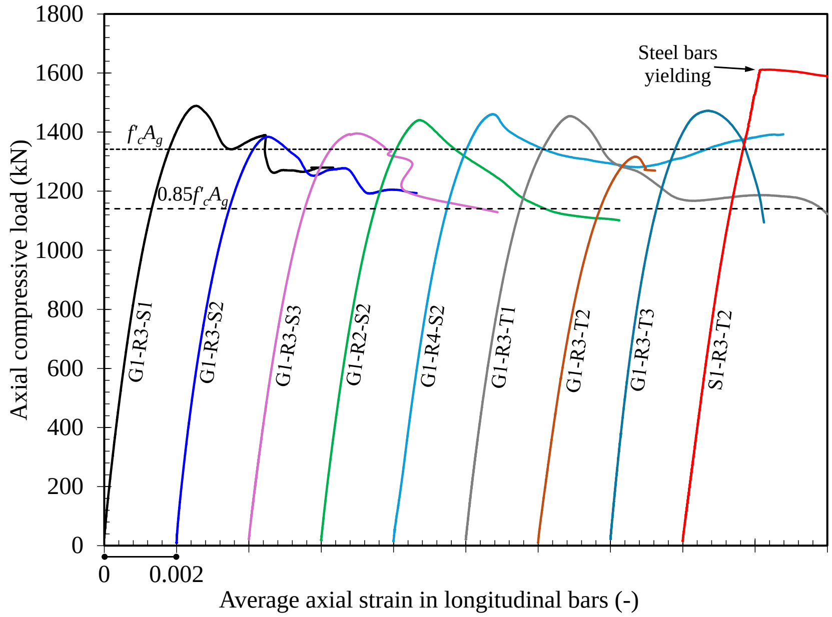

Figure 12 – Load versus axial strain in bars for specimens under concentric load

Figure 13 compares the axial strain in the longitudinal bars versus axial compressive load for specimens with GFRP spirals under concentric and eccentric loading. As load eccentricity increased, the strains at a specific load level before peak load increased as well, indicating a reduction in axial stiffness due to the involvement of bending moments in the section. For concentric loading, the impact of spiral pitch on the ascending branch of the diagram is minimal, with a slight difference where nonlinearity in strains begins at higher loads for specimens with a smaller pitch.

Under low eccentricity (e=15%), this difference remains negligible, as the specimens exhibited nearly identical peak loads, and the compression-side diagrams overlap. However, on the tension side, specimens with a smaller spiral pitch showed higher strains at a given load level, indicating more involvement of the longitudinal reinforcement in bending. As eccentricity increases to moderate values (e=30%), this trend is observed on both the compression and tension sides. Specimens with a smaller pitch experienced higher strains, likely due to the greater integrity of the reinforcement, which promotes a more uniform stress distribution across the section and increases the involvement of the longitudinal bars.

The strain development in the longitudinal bars becomes more pronounced as eccentricity increases. As shown in the figure, disregarding strain gauge failures, the strains in the bars increase from around 0.007 for concentric loading to over 0.010 under low eccentricity (15%) and exceed 0.015 under moderate eccentricity (30%).

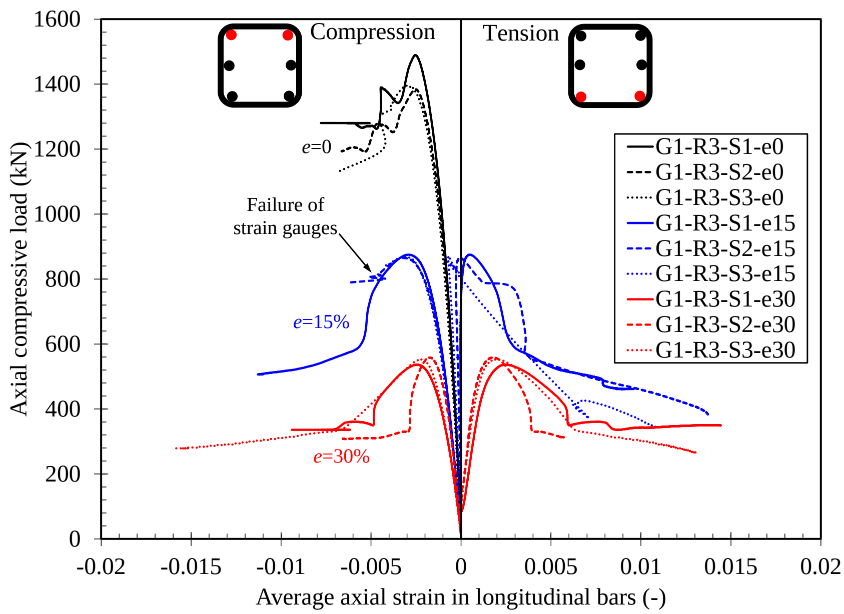

Figure 13 – Load versus axial strain in bars under eccentric load

3.2.4. Transverse reinforcement Strain

Figure 14 shows that positive strains were recorded for the strain gauges placed on the sides of the spiral, while negative strains were recorded for those on the corners. This indicates that, while the sides of the section are in tension, the corners are under compression, which aligns with the expected stress distribution pattern in confined concrete within a square cross-section.

The strains on the tension side are more developed at lower eccentricity levels, while strain development on the compression side increased with higher eccentricity. For concentric loading, the strains on the tension side reached approximately 0.006, while for eccentric loading (15% and

30%), they developed to around 0.004. These values do not represent the maximum strain capacity of the spirals but rather the highest recorded strains before column failure or strain gauge malfunction.

This suggests that spirals remained effective and continued to confine the core until the failure of the longitudinal bars. Observations of the failure patterns confirmed that there was no visible damage to the spirals until the longitudinal bars failed. The only noted failure in the spiral occurred in a specimen under eccentric loading, which happened well after the longitudinal bars had failed. This emphasizes the continued functionality of the spirals in maintaining structural integrity up to the point of failure.

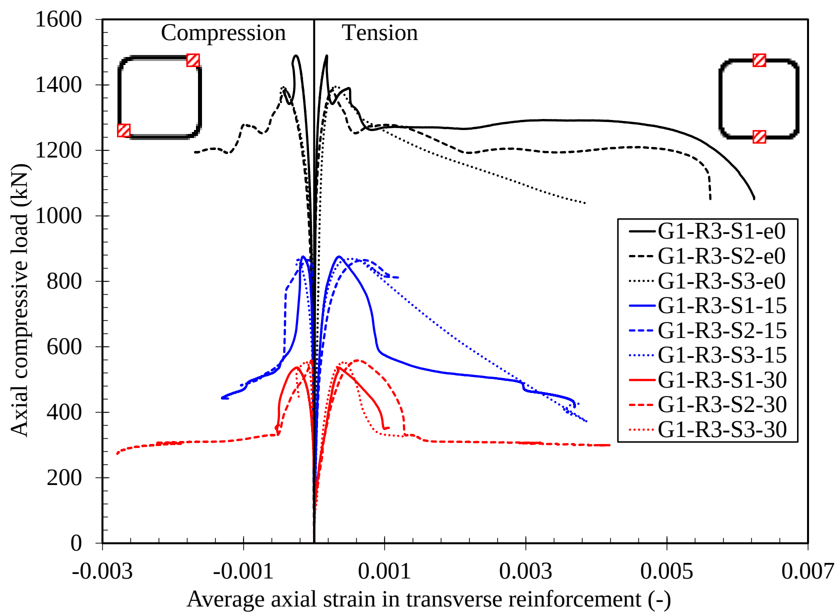

Figure 14 – Load versus strain in spirals under eccentric load

Figure 15 offers a clear view of the progression of events during testing under concentric load, allowing for a comparison of the behavior of spiral and tie reinforcement at each stage of loading. As shown, the effect of confinement becomes increasingly significant as the columns approach failure. Specimens with smaller spiral pitches or tighter tie spacing demonstrated higher axial strains, indicating that the reinforcement remains effective up to failure. For instance, in specimens with the smallest spiral pitch (S1) and the tightest tie spacing (T1), the transverse reinforcement maintained its structural integrity for a longer duration, allowing the concrete core to endure higher strains before collapsing. On the other hand, specimens with larger spiral pitches or wider tie spacings (S3 and T3) exhibit lower strain levels at failure.

Regarding the stress states in longitudinal and transverse reinforcement, stresses in the transverse reinforcement remained minimal until the peak load, especially when compared to the longitudinal reinforcement. The longitudinal bars contributed to load-bearing from the beginning up to failure, while the transverse reinforcement primarily engaged in confining the concrete core after it begins to expand, which occurs mostly after the peak load is reached.

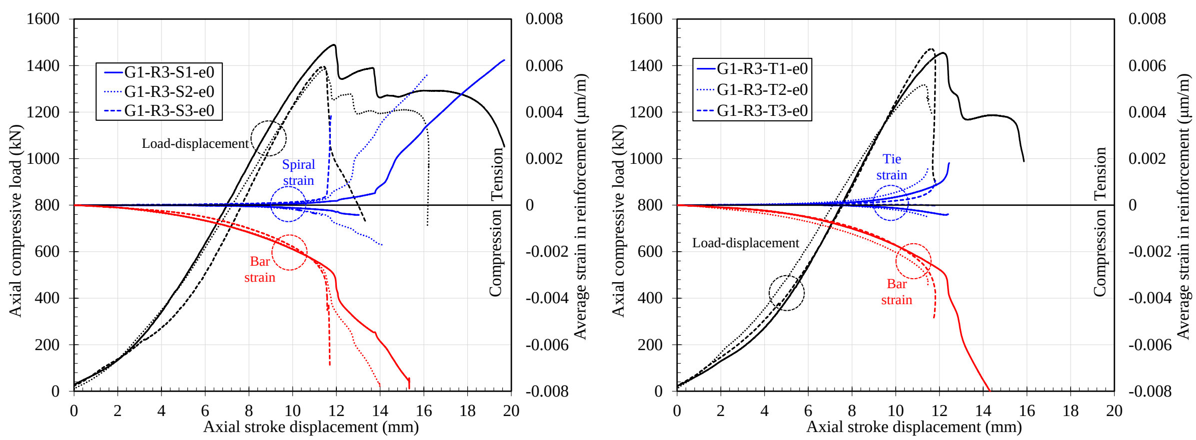

Figure 15 – Comparison of strains in spirals and ties under eccentric load together with longitudinal bars strain and load-displacement behavior

3.2.5. Volumetric strain

As concrete approaches its uniaxial strength, microcracks begin to propagate, and the concrete core starts to expand laterally under axial compression. This outward bulging activates the transverse reinforcement, causing stress to develop in the confining elements. As a result, passive confinement becomes effective, introducing a triaxial stress state within the concrete. At this stage, the volumetric strain, ε_v, is defined in terms of the axial strain, ε_{ax}, and lateral strain, ε_{lat}:

$$\varepsilon_v = \varepsilon_{ax} + 2\varepsilon_{lat} \quad (1)$$

The relationship between volumetric strain and axial strain for various specimens is depicted in Figure 16. Positive volumetric strain indicates contraction, while negative strain reflects expansion. Prior to reaching the peak load, the data follows a straight line represented by $\varepsilon_v = 0.6\varepsilon_{ax}$, where the coefficient 0.6 is derived from a Poisson's ratio, ν, of 0.2. The longer a specimen remains along this line, the higher the concentration of transverse reinforcement it possesses, which delays lateral expansion to higher axial strain levels. As microcracks propagate and the concrete core begins to expand, the graph deviates from this line and shows greater expansion, similar to observations made by De Luca et al. [2], Tobbi et al. [17], and Mohamed et al. [9] for ties, hoops, and spirals. The data indicates that square spirals were more effective in controlling the onset of lateral expansion.

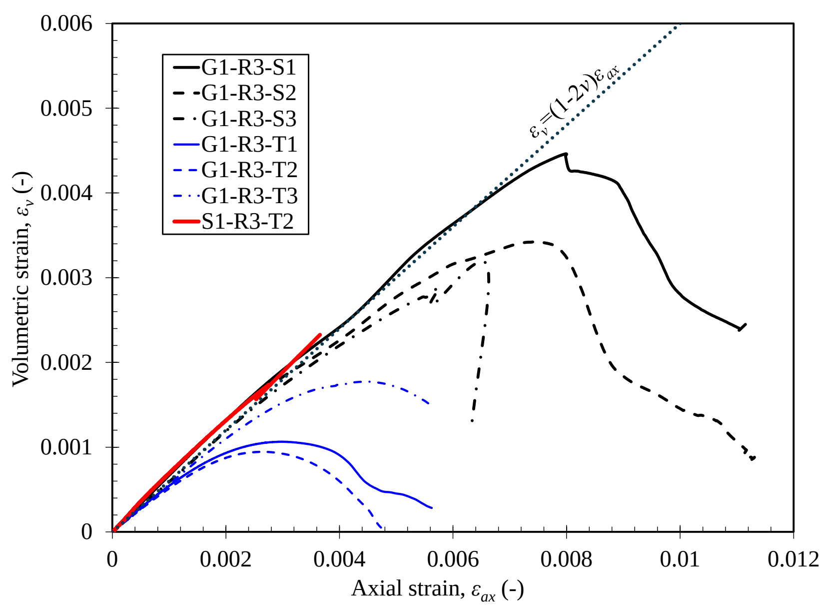

Figure 16 - Volumetric strain, ε_v, versus axial strain, ε_{ax}, for specimens with varying tie and spiral configurations

4. ANALYTICAL STUDY

4.1. Model Description

The analytical model developed in this study is capable of performing both section analysis and second-order analysis of GFRP-RC columns under varying eccentricities.

4.1.1. Section Analysis

The axial force and bending moment capacities are calculated based on the geometry of the column, including its dimensions, cover, and the size and location of the GFRP bars. The material properties of concrete and GFRP are defined, where the ultimate strain in concrete is taken as ε_{cu}=0.003, and the elastic modulus is calculated using $E_c = 4700\sqrt{f_c'}$ for normal strength concrete [23], and $E_c = 3320\sqrt{f_c'} + 6900$ for high-strength concrete [30]. The contribution of GFRP bars in compression is taken into account, as previous research by the authors and other researchers has shown that the compressive modulus of GFRP is nearly equal to its tensile modulus, and its compressive strength is significant enough to warrant consideration [25], [31], [32], [33], [34], [35], [36]. Their elastic modulus, tensile, and compressive strengths are specified, and the ultimate strains in tension, ε_{ftu}, and compression, ε_{fcu}, are computed, assuming linear elastic behavior up to failure.

The analysis begins with an initial assumption that the neutral axis, C_{NA}, is located at the mid-height of the column. This assumption is iteratively refined based on the difference between the calculated axial force, P_n, and the applied load, P. For each load increment, the strain in the GFRP bars is determined using strain compatibility within the section, and the stress in each bar is derived assuming linear elastic behavior. The axial force and moment contributions from each layer of bars, F_{fi} and M_{fi}, are then computed based on the cross-sectional area of the bars. The overall axial force, F_f, and moment, M_f, are obtained by summing the contributions from all layers.

For the normal strength concrete, Popovics' model [37] is used to represent the nonlinear stress-strain relationship:

$$f_c = f_c' \frac{\varepsilon_c}{\varepsilon_c'} \frac{n}{n - 1 + \left(\frac{\varepsilon_c}{\varepsilon_c'}\right)^n} \tag{2}$$

The strain corresponding to the peak stress is calculated as $\varepsilon_c' = 1.7\, f_c'/E_c$, and the parameter n is defined by the ratio between the modulus of elasticity and the stress-strain response, $E_c/(E_c - f_c'/\varepsilon_c')$. For high-strength concrete, Thorenfeldt's model [38] was used in which a factor $k = 0.67 + f_c'/62$, is included in the formula to modify the descending branch of the concrete stress-strain curve:

$$f_c = f_c' \frac{\varepsilon_c}{\varepsilon_c'} \frac{n}{n - 1 + \left(\frac{\varepsilon_c}{\varepsilon_c'}\right)^{nk}} \tag{3}$$

The tensile strength of concrete and the tension stiffening effects are neglected for simplicity. The concrete section is discretized into fibers on the compressive side, and the stress in each fiber is calculated based on its strain, excluding the areas occupied by the bars. The axial force, F_{cj}, and moment, M_{cj}, contributions from each fiber are computed, and the overall force, F_c, and moment, M_c, for the concrete are summed.

For each load increment, the model iterates to find the neutral axis, C_{NA}, that satisfies force equilibrium such that the sum of the axial forces in the concrete and bars, $P_n=F_c+F_f$, matches the applied load P. The bending moment, $M_n=M_c+M_f$, is then calculated about the neutral axis. The interaction diagram is generated by plotting the P_n and M_n pairs for each load step. The internal load eccentricity is defined as $e=M_n/P_n$, and the curvature is computed as ε_{cm}/C_{NA}. These results are stored in a moment-curvature matrix for use in the second-order analysis.

4.1.2. Second-Order Analysis

The second-order analysis is based on data from the moment-curvature relationships obtained in the section analysis. The column length, L, and the load eccentricity, e, which affects the column's load-deflection behavior, are specified. The deflected shape of the column is approximated as a sine curve, with an initial assumption for the mid-length deflection. An iterative process is then used to refine the deflection values at the mid-height of the column, starting with three nodes: one at the mid-height and two at the ends.

For each load increment, the total eccentricity is calculated by adding the initial eccentricity, e, to the deflection-induced eccentricity, δ. The corresponding moment is then calculated as $M_n=P\times(e+\delta)$, where P is the applied axial load. Using the previously developed moment-curvature matrix, the curvatures at the ends of the column, ϕ_0, and at mid-height, ϕ_m, are determined. The moment-area theorem is applied, assuming a half-sine shape for the deflected column [6], [39]:

$$\phi(x) = (\phi_m - \phi_0) sin\left(\frac{\pi x}{L}\right) + \phi_0 \quad (4)$$

$$\delta_m = \int_0^{L/2} (L/2 - x)\, \phi(x) dx \quad (5)$$

Where L is the total length of the column. This iterative process continues until the calculated mid-length deflection converges with the assumed deflection within a specified tolerance. For each load step, the curvature and moment data are used to update the deflected shape and determine the strains in the GFRP bars using strain compatibility. The iterative procedure continues until convergence, at which point the final deflection at mid-length is recorded. The process is repeated for each subsequent load increment, with the load increasing until the peak load is reached.

After reaching the peak load, the analysis proceeds to the descending branch of the load-deflection curve, representing the post-peak behavior of the column. During this stage, the axial load is reduced incrementally, and the same iterative process is used to compute the curvature and deflection values. The moment-curvature diagram is used to track the curvatures and moments for both ascending and descending branches, ensuring that the curvature does not decrease during the post-peak analysis. The descending branch provides insight into the ductility and post-peak performance of the column under eccentric loading.

4.2. Model Verification

Two experimental studies on square columns were selected to verify the analytical model's predictions for lateral displacement and longitudinal bar strains. The first verification used Column G1 from Guerin et al. [12], which is 2000 mm in length with a 405 mm square cross section, reinforced with six #6 longitudinal bars, and concrete strength of 40 MPa. This column was tested under eccentricities of 10%, 20%, and 40%. The second study, by Khorramian and Sadeghian [6], involved square columns with a length of 500 mm and cross-sectional side dimensions of 150 mm, reinforced with six #5 longitudinal bars. The concrete strength was 37 MPa, and tests were conducted with 10%, 20%, and 30% load eccentricities.

Figure 17 presents the axial load versus mid-height lateral displacement and axial load versus longitudinal bar strain diagrams, comparing the experimental results from each study with the model predictions. The model demonstrates strong agreement with the experimental data, accurately capturing the diagram's form before peak load, at peak load, and with acceptable correspondence in the post-peak range.

For a more detailed comparison between model predictions and experimental outputs, peak load values and other key parameters at peak load are presented in Table 7. The model predictions closely match the experimental peak load values. The mid-height displacement and strain results also show good agreement with experimental values, showing the model's capability in reproducing the response parameters.

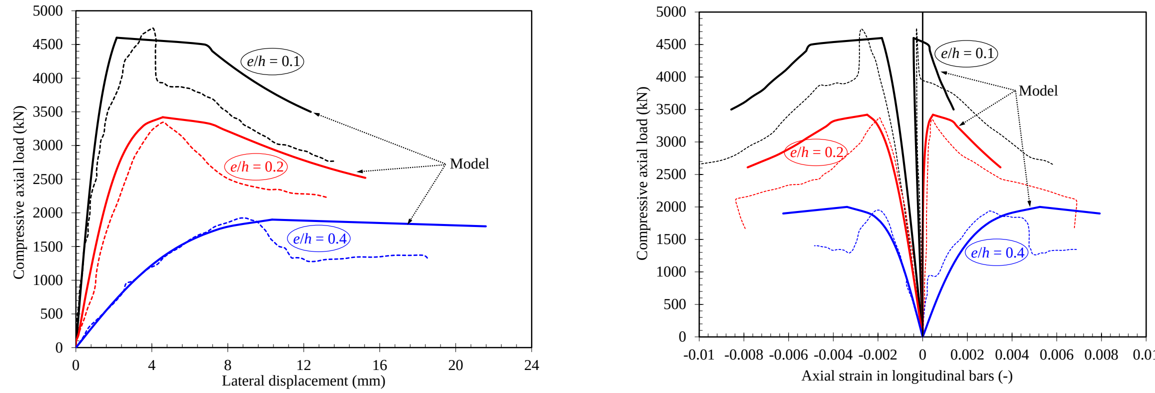

(a)

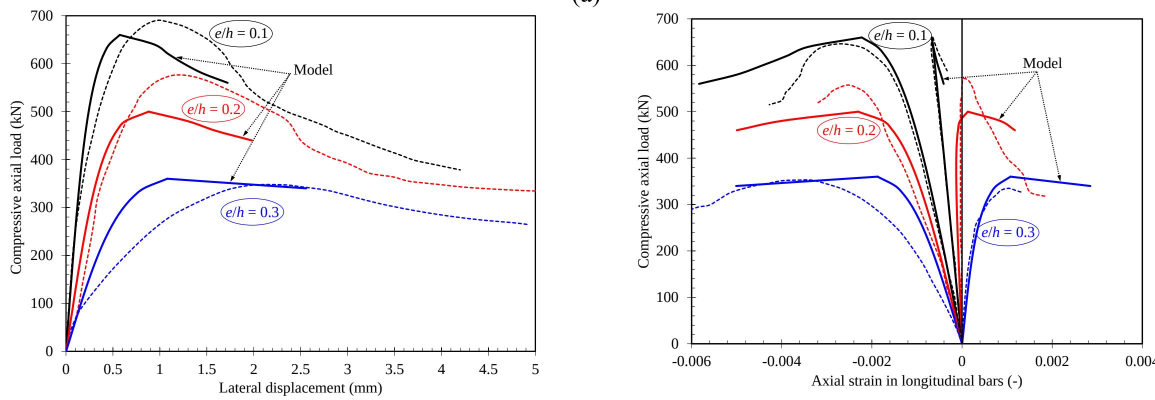

(b)

Figure 17 – Verification of the analytical model compared to test results by a) Guerin et al. [12] and b) Khorramian and Sadeghian [6]

Table 7 – Comparison of the key parameters from code predictions and the literature test results

Study	Parameter*	*e/h*	Test	Model	Error (%)
Guerin et al. [12]	P_{max} (kN)	0.1	4700	4600	2.1
		0.2	3345	3420	-2.2
		0.4	1920	1900	1.0
	δ_m (mm)	0.1	4.2	2.2	49.1
		0.2	4.6	4.6	0.7
		0.4	8.6	10.3	-19.6
	$\varepsilon_{fc,0}$ (-)	0.1	-0.0028	-0.0020	27.3
		0.2	-0.0019	-0.0025	-29.5
		0.4	-0.0020	-0.0034	-73.6
	$\varepsilon_{ft,0}$ (-)	0.1	-0.0003	-0.0004	-46.4
		0.2	0.0004	0.0005	-9.8
		0.4	0.0030	0.0051	-69.4
Khorramian and Sadeghian [6]	P_{max} (kN)	0.1	693	660	4.7
		0.2	578	500	13.5
		0.3	354	360	-1.7
	δ_m (mm)	0.1	0.9	0.6	38.0
		0.2	1.1	0.9	20.7
		0.3	2.0	1.1	46.8
	$\varepsilon_{fc,0}$ (-)	0.1	-0.0028	-0.0023	19.4
		0.2	-0.0029	-0.0023	20.1
		0.3	-0.0036	-0.0019	48.1
	$\varepsilon_{ft,0}$ (-)	0.1	-0.0007	-0.0007	6.9
		0.2	0.0001	0.0001	-50.0
		0.3	0.0012	0.0011	8.5

* All values are presented at peak load

4.3. Test Specimens

In this section, the analytical model's predictions for the behavior of the GFRP-RC columns tested in this study are compared with the experimental results. Figure 18 presents the load-lateral displacement curves from the analytical model alongside the test data. A strong correlation is observed across different loading stages, including pre-peak, peak, and post-peak behavior. The experimental results recorded peak loads of 870 and 550 kN, respectively, while the model calculates peak loads of 880 and 520 kN for eccentricities of 15% and 30%, respectively. The mid-height displacements recorded at peak load in tests are 5.5 and 8.9 mm for 15 and 30% eccentricity, respectively, while the model calculated these values 4.5 and 7.6 mm, respectively. This close alignment indicates the model's accuracy in capturing the structural response of GFRP-RC columns under varying load eccentricities.

The model does not consider the effect of transverse reinforcement; therefore, it cannot see the differences in the post peak for different spiral configurations. Nonetheless, as seen, the experimental outputs indicate that specimens under the same eccentricity had almost similar behavior up to around peak load and after that there are marginal differences regarding the amount of load drop. This means that the model could acceptably simulate the column behavior regardless of the type or configuration of the transverse reinforcement.

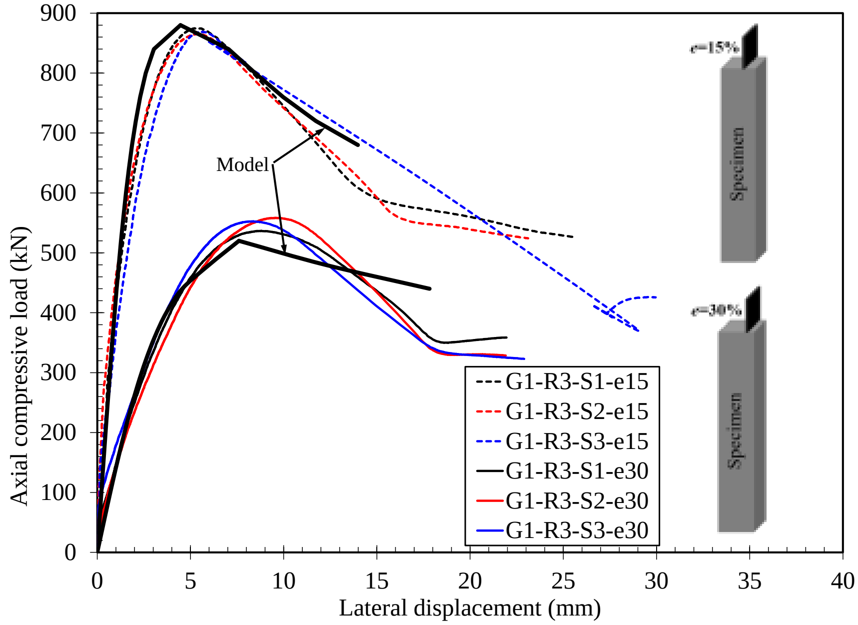

Figure 18 – Analytical model versus the test results of this study for load-lateral displacement

Figure 19 shows load versus longitudinal reinforcement strains for the test specimens and the model. As seen, the bar strains at peak load calculated by the model are in good agreement with the tests results. On the compression side, the bars strains recorded in tests are -0.0031 and -0.0022 for 15 and 30% eccentricity, respectively, while model resulted -0.0022 and -0.0018. On the tension side, tests results are -0.00007 and 0.0021, for 15 and 30% eccentricity, while model calculated them as -0.00007 and 0.0021. These values, especially the tensile strains, show that that model could calculate the strains in good agreement with the tests.

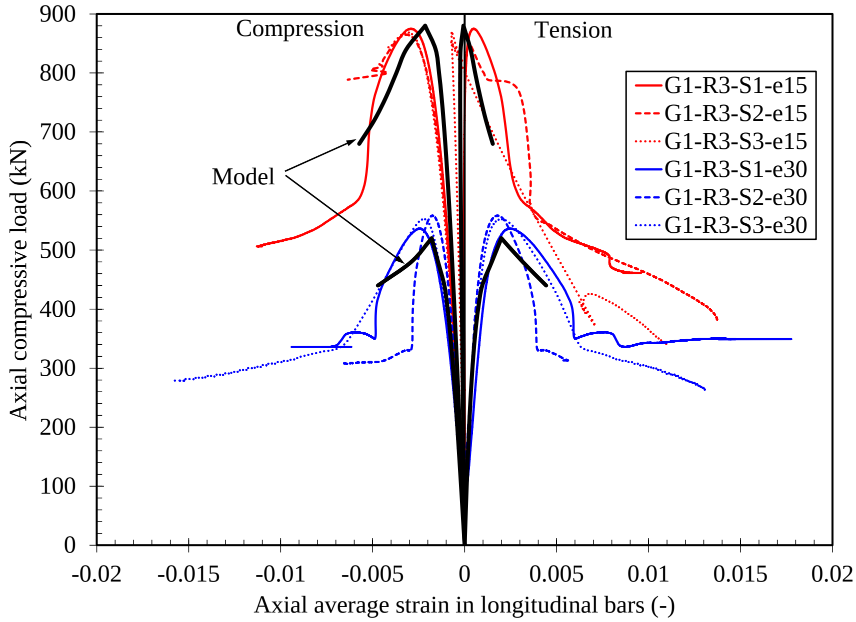

Figure 19 – Analytical model versus the test results of this study for load-bar strain

The column interaction line calculated from the model by including the effect of GFRP bars in compression is shown in Figure 20 together with the loading path for columns under 15 and 30% load eccentricity, respectively. As seen, the interaction line is in good agreement with the data points resulted from the tests. Under concentric loading, the peak load of the columns with denser spiral pitch are higher than the model calculation due to the confinement effect. However, under 15% load eccentricity, test results are lower than the model calculation which can be due to earlier cracks on the cover. This was not the case for 30% load eccentricity which means that when confinement is not in effect under eccentric loading, the higher the eccentricity (the lower the peak load) this reduction effect on strength is less sensible.

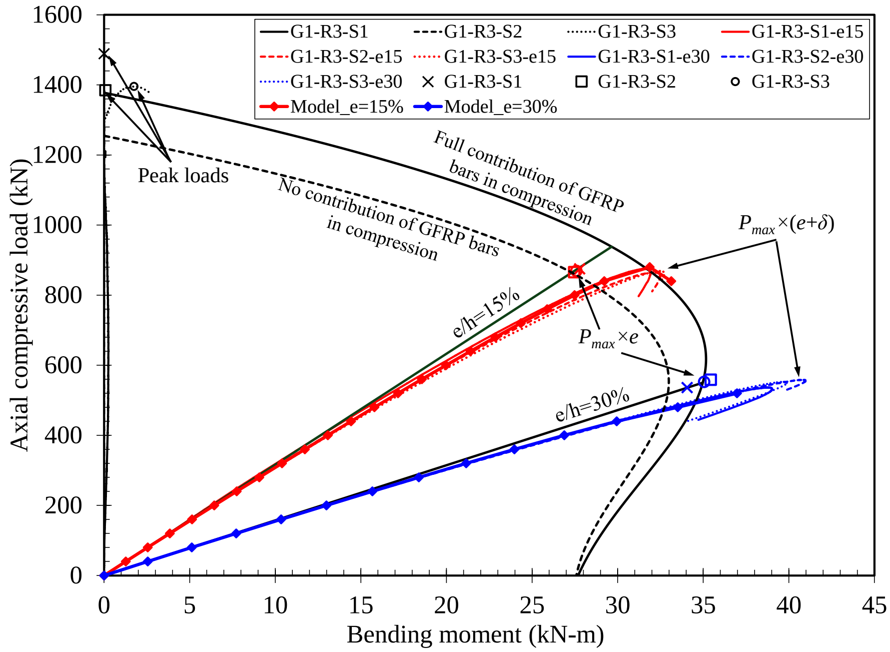

Figure 20 – Analytical model versus the test results of this study for loading path

5. CONCLUSION

This study investigated the effects of square spirals with varying pitches, and square ties with different configurations on the behavior of GFRP-reinforced concrete (GFRP-RC) columns under concentric and eccentric loading. A total of fifteen specimens were tested to examine failure mechanisms and structural response. Additionally, an analytical model was developed to perform section analysis and second-order analysis, accurately predicting deflections, strains, and load paths for eccentrically loaded columns. The model was validated against both the current test results and data from previous studies. The key findings are as follows:

- Under concentric loading, tie-reinforced specimens with a $20d_t$ overlap and a 190 mm ($\approx 12d_b$) spacing exhibited tie opening at peak load. Reducing the tie spacing to 75 mm ($\approx 5d_b$) delayed tie opening to the post-peak phase, while increasing the overlap to $28d_t$ prevented tie failure entirely. Spiral-reinforced specimens did not experience spiral rupture, demonstrating better confinement efficiency.

- Columns with denser spiral reinforcement (50 mm pitch) under concentric loading exhibited a more stable response, with an approximate 7% increase in peak load compared to those with a 75 mm pitch. Similarly, a $28d_t$ tie overlap with 90° hooks and strong fasteners significantly improved tie performance, preventing premature failure. In all spiral-reinforced specimens, longitudinal bar crushing or slippage occurred well after peak load, with spiral failure occurring even later.
- Under concentric loading, the steel-reinforced specimen achieved the highest peak load, with the longitudinal bars contributing approximately 30% of the total load. In GFRP-RC columns, the bars contributed between 7% and 15% of the load, depending on the ratios of longitudinal bars to spirals or ties.
- For spiral reinforcement, a denser 50×50 mm reinforcement mesh, consisting of a 50 mm ($\approx 3d_b$) pitch and eight longitudinal bars covering both the corners and mid-sections (4% reinforcement ratio), enhanced confinement and optimized deformability. This configuration resulted in a second peak load reaching approximately 98% of the initial peak.
- Columns with square spirals, effectively delayed lateral expansion, maintaining a stable volumetric-to-axial strain relationship up to higher axial strains. This provided enhanced confinement as the concrete approached peak load, with the confinement effect increasing with higher concentrations of transverse reinforcement.
- The analytical model demonstrated strong agreement with experimental results, accurately predicting structural behavior across different loading stages. It was verified against square columns with no transverse reinforcement, with ties, and with spirals, showing its capability in capturing the load-displacement response. However, more complex models,

such as finite element simulations, may be required for a detailed post-peak behavior assessment.

ACKNOWLEDGEMENTS

The authors would like to acknowledge the support of the Natural Sciences and Engineering Research Council of Canada (NSERC) for funding this research. Special thanks are extended to PULTRALL Inc. for providing the V-ROD composite bars and spirals used in the study. The authors also wish to express their gratitude to lab technicians Jordan Maerz and Jesse Keane for their invaluable assistance with the experimental setup and testing.

DATA AVAILABILITY STATEMENT

The data will be provided upon reasonable request.

REFERENCES

[1] M. Z. Afifi, H. M. Mohamed, and B. Benmokrane, "Axial capacity of circular concrete columns reinforced with GFRP bars and spirals," *Journal of Composites for Construction*, vol. 18, no. 1, p. 04013017, 2014.

[2] A. De Luca, F. Matta, and A. Nanni, "Behavior of full-scale glass fiber-reinforced polymer reinforced concrete columns under axial load," *ACI Struct J*, vol. 107, no. 5, p. 589, 2010.

[3] A. Hadhood, H. M. Mohamed, and B. Benmokrane, "Experimental study of circular high-strength concrete columns reinforced with GFRP bars and spirals under concentric and eccentric loading," *Journal of Composites for Construction*, vol. 21, no. 2, p. 04016078, 2017.

[4] A. Hadhood, H. M. Mohamed, F. Ghrib, and B. Benmokrane, "Efficiency of glass fiber-reinforced polymer (GFRP) discrete hoops and bars in concrete columns under combined axial and flexural loads," *Compos B Eng*, vol. 114, pp. 223–236, 2017.

[5] M. N. S. Hadi, H. A. Hasan, and M. N. Sheikh, "Experimental investigation of circular high-strength concrete columns reinforced with glass fiber-reinforced polymer bars and helices under different loading conditions," *Journal of Composites for Construction*, vol. 21, no. 4, p. 04017005, 2017.

[6] K. Khorramian and P. Sadeghian, "Experimental and analytical behavior of short concrete columns reinforced with GFRP bars under eccentric loading," *Eng Struct*, vol. 151, pp. 761–773, 2017, doi: https://doi.org/10.1016/j.engstruct.2017.08.064.

[7] M. N. S. Hadi, H. Karim, and M. N. Sheikh, "Experimental investigations on circular concrete columns reinforced with GFRP bars and helices under different loading conditions," *Journal of Composites for Construction*, vol. 20, no. 4, p. 04016009, 2016.

[8] G. B. Maranan, A. C. Manalo, B. Benmokrane, W. Karunasena, and P. Mendis, "Behavior of concentrically loaded geopolymer-concrete circular columns reinforced longitudinally and transversely with GFRP bars," *Eng Struct*, vol. 117, pp. 422–436, 2016.

[9] H. M. Mohamed, M. Z. Afifi, and B. Benmokrane, "Performance evaluation of concrete columns reinforced longitudinally with FRP bars and confined with FRP hoops and spirals under axial load," *Journal of Bridge Engineering*, vol. 19, no. 7, p. 04014020, 2014.

[10] M. Elchalakani and G. Ma, "Tests of glass fibre reinforced polymer rectangular concrete columns subjected to concentric and eccentric axial loading," *Eng Struct*, vol. 151, pp. 93–104, 2017.

[11] L. Sun, M. Wei, and N. Zhang, "Experimental study on the behavior of GFRP reinforced concrete columns under eccentric axial load," *Constr Build Mater*, vol. 152, pp. 214–225, 2017.

[12] M. Guérin, H. M. Mohamed, B. Benmokrane, C. K. Shield, and A. Nanni, "Effect of Glass Fiber-Reinforced Polymer Reinforcement Ratio on Axial-Flexural Strength of Reinforced Concrete Columns.," *ACI Struct J*, vol. 115, no. 4, 2018.

[13] M. Guérin, H. M. Mohamed, B. Benmokrane, A. Nanni, and C. K. Shield, "Eccentric Behavior of Full-Scale Reinforced Concrete Columns with Glass Fiber-Reinforced Polymer Bars and Ties.," *ACI Struct J*, vol. 115, no. 2, 2018.

[14] A. Hadhood, H. M. Mohamed, and B. Benmokrane, "Axial load–moment interaction diagram of circular concrete columns reinforced with CFRP bars and spirals: Experimental and theoretical investigations," *Journal of Composites for Construction*, vol. 21, no. 2, p. 04016092, 2017.

[15] M. Z. Afifi, H. M. Mohamed, and B. Benmokrane, "Strength and axial behavior of circular concrete columns reinforced with CFRP bars and spirals," *Journal of Composites for Construction*, vol. 18, no. 2, p. 04013035, 2014.

[16] M. Z. Afifi, H. M. Mohamed, O. Chaallal, and B. Benmokrane, "Confinement model for concrete columns internally confined with carbon FRP spirals and hoops," *Journal of Structural Engineering*, vol. 141, no. 9, p. 04014219, 2015.

[17] H. Tobbi, A. S. Farghaly, and B. Benmokrane, "Concrete Columns Reinforced Longitudinally and Transversally with Glass Fiber-Reinforced Polymer Bars.," *ACI Struct J*, vol. 109, no. 4, 2012.

[18] H. Tobbi, A. S. Farghaly, and B. Benmokrane, "Behavior of Concentrically Loaded Fiber-Reinforced Polymer Reinforced Concrete Columns with Varying Reinforcement Types and Ratios.," *ACI Struct J*, vol. 111, no. 2, 2014.

[19] H. Tobbi, A. S. Farghaly, and B. Benmokrane, "Strength model for concrete columns reinforced with fiber-reinforced polymer bars and ties," *ACI Struct J*, vol. 111, no. 4, pp. 789–798, 2014.

[20] M. A. Ali and E. El-Salakawy, "Seismic performance of GFRP-reinforced concrete rectangular columns," *Journal of Composites for Construction*, vol. 20, no. 3, p. 04015074, 2016.

[21] H. Karim, B. Noel-Gough, M. N. Sheikh, and M. N. S. Hadi, "Strength and ductility behavior of circular concrete columns reinforced with GFRP bars and helices," in *The 12th International Symposium on Fiber Reinforced Polymers for Reinforced Concrete Structures (FRPRCS-12)*, 2015.

[22] ASTM, “ASTM C39 / C39M, Standard Test Method for Compressive Strength of Cylindrical Concrete Specimens,” 2021.

[23] ACI, *ACI CODE-440.11-22: Building Code Requirements for Structural Concrete Reinforced with Glass Fiber-Reinforced Polymer (GFRP) Bars-Code and Commentary*. American Concrete Institute, 2022.

[24] ASTM, *ASTM D7205/D7205M, Standard Test Method for Tensile Properties of Fiber-Reinforced Polymer Matrix Composite Bars*. 2021.

[25] A. Sadat Hosseini and P. Sadeghian, “Assessing Compressive Properties of GFRP Bars: Novel Test Fixture and Statistical Analysis,” *Journal of Composites for Construction*, vol. 29, no. 2, p. 04025011, 2025.

[26] K. Khorramian and P. Sadeghian, “Experimental investigation of short and slender rectangular concrete columns reinforced with GFRP bars under eccentric axial loads,” *Journal of Composites for Construction*, vol. 24, no. 6, p. 04020072, 2020.

[27] ACI, *ACI 318-19: Building Code Requirements for Structural Concrete and Commentary*. American Concrete Institute, 2019.

[28] W. Abdelazim, H. M. Mohamed, B. Benmokrane, and M. Z. Afifi, “Effect of critical test parameters on behavior of glass fiber-reinforced polymer-reinforced concrete slender columns under eccentric load,” *ACI Struct J*, vol. 117, no. 4, pp. 127–141, 2020.

[29] A. Hadhood, H. M. Mohamed, F. Ghrib, and B. Benmokrane, “Efficiency of glass-fiber reinforced-polymer (GFRP) discrete hoops and bars in concrete columns under combined axial and flexural loads,” *Compos B Eng*, vol. 114, pp. 223–236, 2017.

[30] ACI, *ACI PRC-363-10 Report on High-Strength Concrete*. American Concrete Institute, 2010.

[31] K. Khorramian and P. Sadeghian, “Material characterization of GFRP bars in compression using a new test method,” *J Test Eval*, 2019.

[32] B. Fillmore and P. Sadeghian, “Contribution of longitudinal glass fiber-reinforced polymer bars in concrete cylinders under axial compression,” *Canadian Journal of Civil Engineering*, vol. 45, no. 6, pp. 458–468, 2018.

[33] O. S. AlAjarmeh, A. C. Manalo, B. Benmokrane, P. V Vijay, W. Ferdous, and P. Mendis, “Novel testing and characterization of GFRP bars in compression,” *Constr Build Mater*, vol. 225, pp. 1112–1126, 2019.

[34] T. D’Antino and M. A. Pisani, “Tensile and compressive behavior of thermoset and thermoplastic GFRP bars,” *Constr Build Mater*, vol. 366, p. 130104, 2023.

[35] A. S. Hosseini, S. K. Velkumar, and P. Sadeghian, “Behavior of GFRP-Reinforced Concrete Members under Combined Bending Moment and Low Axial Load,” *Journal of Composites for Construction*, vol. 28, no. 4, p. 04024025, 2024.

[36] L. Bujotzek, D. Beck, E. Apostolidi, and D. Waldmann, “Experimental and statistical investigations of the material properties of FRP reinforcement in compression,” *Constr Build Mater*, vol. 414, p. 134782, 2024.

[37] S. Popovics, "A numerical approach to the complete stress-strain curve of concrete," *Cem Concr Res*, vol. 3, no. 5, pp. 583–599, 1973.

[38] E. Thorenfeldt, "Mechanical properties of high-strength concrete and applications in design," in *Symposium Proceedings, Utilization of High-Strength Concrete, Norway, 1987*, 1987.

[39] A. Mirmiran, W. Yuan, and X. Chen, "Design for slenderness in concrete columns internally reinforced with fiber-reinforced polymer bars," *Structural Journal*, vol. 98, no. 1, pp. 116–125, 2001.